Narodowe Centrum Badań Jądrowych
National Centre for Nuclear Research
ŚWIERK

High-temperature corrosion of ceramic construction materials for Dual Fluid Reactor

Michał Komorowicz

A thesis submitted in fulfilment of the requirements for the degree of Doctor of Physical Sciences in Department of Complex System

Supervisor:
Prof. Dr. Hab. Konrad Czerski

Auxiliary supervisor:
Dr. Kazimierz Skrobas

Otwock 2023

Acknowledgments

I would like to sincerely thank my supervisor, Professor Konrad Czerski, for his patience, expert guidance, and immense support, throughout my doctoral journey.

I would also like to express my gratitude to my auxiliary supervisor, Dr. Kazimierz Skrobas, and his wife, Dr. Kamila, for their guidance, continuous assistance, and always being available to help.

A special thanks goes to my friends from the PhD4GEN project for their support, especially to Mateusz for all those battles against the rebellious machines.

Lastly, I am truly grateful to my family and my beloved Karolina for their unwavering support and belief in me.

Contents

Author's Contribution 7
List of Figures 9
Acronyms 10
Abstrakt 12
Streszczenie 13
I Introduction 14
1.1 Motivation 14
1.2 Objective of the thesis 14
1.3 Research hypothesis 14
1.4 Outline 15
II Dual Fluid Reactor technology 16
2.1 Concept Overview 17
2.2 Structural material 18
2.3 Production methods 19
2.4 Coolant 21
2.5 Metallic fuel 22
III Corrosion 23
3.1 Corrosion mechanisms 23
3.2 Corrosion by lead 24
3.3 Oxidation and influence of oxide layer 25
3.4 Interactions with uranium and chromium 28
3.5 Interactions with other impurities 30
3.6 Limitation of corrosion effects 30
IV Simulations 32
4.1 Density Functional Theory calculations 32
4.2 Methodology 33
4. 3 Results 36
(100) Surface 36
(110) Surface 39
(111) Surface 40
4.4 Analysis and discussion 45
4.5 Molecular dynamics simulations 46
4.6 Methodology 46

4.7 Results 48
4.8 Analysis and discussion 53
V Microdemonstrator loop 54
5.1 Experiment facility details 55
5.2 Main tank 56
5.3 Heat exchanger 57
5.4 Expansion tanks 58
5.5 Radiator 58
5.6 Pumping system 59
5.7 Sensors 60
5.8 Oxygen measurements and composition control 62
5.9 Corrosion Experiment Description 63
5.10 Preparation and control of experiment 63
5.11 Analysis and discussion 64
VI Summary 65
References 66

Author's Contribution

The present thesis is based on the publication below:

Komorowicz M.; Skrobas K.; Czerski K. *First-Principles Study of Adsorption of Pb Atoms on 3C-SiC* in the Materials 2023, 16(20), 6700; https://doi.org/10.3390/ma16206700

List of Figures

Figure 1: DFR fuel and cooling loop layout
Figure 2: Single crystal cell of 3C-SiC
Figure 3: Ellingham diagram of oxides
Figure 4: Dependence of the reactions equilibrium on the temperature and the partial pressure of oxygen
Figure 5: Ellingham diagram of carbides
Figure 6: Fitting of Birch–Murnaghan isothermal equation
Figure 7: Initial sites of Pb on SiC(100) surface: LB, T, SB, B, H
Figure 8: Top and side view of CDD visualization of C-face, left with isosurface of 2.8 me/Å3 and Si-face, right with 1.9 me/Å3 of (100) plane 1/4 ML, for both SB adsorption site.
Figure 9: Top view of (110) surface with final relaxation positions, HC nearly above C from bottom row closest to two C atoms from top row, Hsi closest to Si and B above atoms from top row
Figure 10: CDD of (110) plane at 1/4 ML HC position, side, and top views
Figure 11: The honeycomb structure (1/2 ML) and he hexagonal structure (3/4 ML) on the C-face of (111) surface, with corresponding CDD graphs
Figure 12: Top and side view of (111) surface CDD, C-face in position hcp and Si-face in fcc
Figure 13: Band structure of a) clear (111) C-face and b) with adatom c) clear (111) Si-face d) with adatom
Figure 14: Partial density of states for bulk crystal, and (111) surface: C-face , C-face with adatom, Si-face, and Si-face with adatom
Figure 15: Utilized Lennard-Jones potentials
Figure 16: Surfaces after minimization
Figure 17: Second (111) plane cut
Figure 18: Fitting of diffusion coefficient to change of MSD in time
Figure 19: Arrhenius equation fitting
Figure 20: Rate of change in diamond structure number in time for different temperatures
Figure 21: Cross section of SiC crystal embedded in Pb, before simulation, after 5 ns and after 10 ns
Figure 22: Project of microdemonstrator loop facility
Figure 23: Main tank cross-section
Figure 24: Heat-exchanger cross-section
Figure 25: Heat radiator with adjustable fins
Figure 26: Magnetic pump
Figure 27: Top view of heat-exchanger

Acronyms

DFR	**Dual Fluid Reactor**
EROI	**Energy Return on Investment**
SiC	**Silicon Carbide**
SiCf/SiC	**SiC fibre-reinforced SiC ceramic matrix**
CVD	**Chemical vapour deposition**
CVI	**Chemical vapour infiltration**
NITE	**Nano-infiltration and transient eutectic phase**
DFT	**Density Functional Theory**
MD	**Molecular Dynamics**
LDA	**Local Density Approximation**
GGA	**Generalized Gradient Approximation**
SCF	**Self-consistent field**
PAW	**Projector Augmented-Wave**
PBE	**Perdew-Burke-Ernzerhof**
CDD	**Charge density difference**
ML	**Monolayer coverage**
NSCF	**Non-self-consistent field**
PDOS	**Partial density of states**
µD	**Micro-demonstrator**
mD	**Mini-demonstrator**

Abstract

The new Dual Fluid Reactor is a technology with great potential, beyond generating electrical energy efficiently, it also produces high temperatures needed for the chemical industry, including hydrogen production. Its unique online fuel processing method opens substantial possibilities for isotope acquisition. The utilization of liquid fuel eliminates many limitations compared to other reactor types, such as the need for fuel shuffling, required high pressure, or stress exerted on fuel rods, all while ensuring a range of passive safety measures. As a result, the reactor's design can be substantially smaller, and with the possibility to reuse spent fuel, it ensures economic attractiveness. However, the high temperature and radiation create exceptionally challenging conditions for materials.

The chosen construction material is refractory silicon carbide ceramic. This highly robust material has proven its potential across various technological fields, driving research forward to better forms, such as composite materials. The fibre matrix provides high mechanical resistance, while advanced methods of filling and coating offer high corrosion resistance. This material is also of interest in fusion research, providing studies on lead alloy in conditions similar to those expected in the reactor. The material exhibits several polymorphic forms, which will coexist under such conditions. Due to other applications and simpler production processes, the α–SiC forms are of greater interest. However, the β–SiC form shows more suitable values of desired properties, necessitating further research to confirm its superiority in this field as well.

This thesis presents the characteristics of the reactor, fuel materials, coolant, and structural material, providing potential paths for their mutual reactions at high temperatures. Molecular dynamics and Density Functional Theory simulations were employed for an in-depth examination of the interactions between 3C-SiC and lead, revealing differences compared to other polymorphic forms and suggesting lower resistance. Experimental validation is necessary to confirm these model's findings. The characteristics and requirements of the currently developed research unit have been presented, which, among other objectives, aims to conduct such corrosion tests.

Streszczenie

Nowy reaktor Dwu Płynowy to technologia z wysokim potencjałem, poza wydajnym generowaniem energii elektrycznej, wytwarza również wysokie temperatury, niezbędne dla przemysłu chemicznego, co obejmuje również produkcję wodoru. Jego unikalna metoda przetwarzania paliwa online otwiera szerokie możliwości pozyskiwania izotopów. Wykorzystanie ciekłego paliwa eliminuje wiele ograniczeń w porównaniu z innymi typami reaktorów, takich jak potrzeba sortowania paliwa, wymagane wysokie ciśnienie czy naprężenia wywierane na pręty paliwowe, jednocześnie zapewniając szereg pasywnych zabezpieczeń. W rezultacie konstrukcja reaktora może być znacznie mniejsza, a możliwość ponownego wykorzystania wypalonego paliwa zapewnia wysoką atrakcyjność ekonomiczną. Jednakże wysoka temperatura i promieniowanie stwarzają wyjątkowo trudne warunki dla materiałów.

Wybranym materiałem konstrukcyjnym jest ceramiczny węglik krzemu. Ten wysoce odporny materiał udowodnił swój potencjał w wielu dziedzinach technologicznych, stymulując badania nad coraz to nowszymi i bardziej zaawansowanymi formami, takimi jak materiały kompozytowe. Matryca z włókien zapewnia wysoką odporność mechaniczną, natomiast zaawansowane metody wypełnienia i powlekania oferują wysoką odporność korozyjną. Materiał ten jest także przedmiotem zainteresowania w badaniach nad fuzją, dostarczając danych dotyczących stopu ołowiu w warunkach zbliżonych do oczekiwanych w reaktorze. Materiał ten występuje w kilku formach polimorficznych, które będą koegzystować w takich warunkach. Ze względu na inne zastosowania i prostsze procesy produkcyjne, formy α-SiC cieszą się większym zainteresowaniem. Jednak forma β-SiC wykazuje bardziej odpowiednie wartości pożądanych właściwości, przez co konieczne są dalsze badania w celu potwierdzenia jej przewagi także w tej dziedzinie.

Niniejsza praca przedstawia charakterystykę reaktora, materiałów paliwowych, chłodziwa oraz materiału konstrukcyjnego, ukazując potencjalne ścieżki ich wzajemnych reakcji w wysokich temperaturach. Do dogłębnej analizy interakcji między 3C-SiC a ołowiem wykorzystano symulacje dynamiki molekularnej oraz teorię funkcjonału gęstości. Badania ujawniły różnice w stosunku do innych form polimorficznych, sugerując niższą odporność. Weryfikacja eksperymentalna jest konieczna do potwierdzenia wyników tych modeli. Przedstawiono także charakterystykę i wymagania powstającej jednostki badawczej, która ma na celu, między innymi, przeprowadzenie takich testów korozyjnych.

I Introduction

1.1 Motivation

In the challenging and dynamic environment of the DFR reactor, corrosion can proceed through numerous, often interrelated processes, which can unfold in various ways depending on the location in the loops. Although the concept is based on well-developed technologies, it employs higher operating parameters, and an unusual material and form of fuel. The high temperature of 1000°C significantly influences the chemical equilibrium of the system, normally non-reactive lead becomes active, and compounds such as carbides and silicides, not occurring in other reactors, emerge. Moreover, other requirements like high purity of components, strictly controlled protective atmosphere, and necessary precautions with toxic metals, and even the need for radiation shielding, significantly complicate the conduction of experiments. Nevertheless, to guarantee safe operation, comprehensive research in this area is essential. One such unit, the double liquid metal microdemonstrator of the reactor, is the currently under development. This multifunctional unit will serve to conduct corrosion tests on both monocrystals, ready samples of the final product, and irradiated samples. For a better understanding of the mechanisms controlling the corrosion processes, it is necessary to conduct simulations describing interactions at the nanoscale, such as molecular dynamics and density functional theory calculations. These methods allow for the precise determination of the dominant mechanisms, and the activation energy of these processes.

1.2 Objective of the thesis

The research goal of this work is to determine the surface of the 3C-SiC crystal most resistant to lead-induced corrosion by means of DFT calculations. Additionally, a molecular dynamics simulations allow for the identification of the dominant mechanism of this interaction and the rate of its change. The scope also includes the design of the experimental loop, that is, the selection of individual components that comply with safety standards and temperature ranges.

1.3 Research hypothesis

The cubic silicon carbide, plane (111) has a similar structural arrangement to the (0001) surface of hexagonal crystals, therefore the adsorption energy of lead atoms will be similar, and the surface terminated with C is more energetically stable. Surfaces (100) and (110), with lower density exhibit less stability in relation with lead. The SiC_f/SiC composite is suitable for use in the DFR reactor.

1.4 Outline

The dissertation consists of five main parts.

The first part presents the theoretical background of DFR technology and characteristics of the selected materials, fuel – uranium-chromium eutectic, coolant – lead and structural material – silicon carbide, with details of the most significant production methods.

The next section focuses on the mutual interactions of these materials and possible contaminants. The main corrosion mechanisms in liquid flowing metal are presented, with special attention paid to oxidation corrosion. It concludes with proposed ways to mitigate this phenomenon.

The third section provides a description of the performed simulations. It is divided into two parts, the first presents the calculations of the adsorption energies of the lead atoms and its influence on the electronic structure of different crystal planes, the second is a description of molecular dynamics simulations of the interaction with this element at high temperature.

The final part is a summary of theoretical findings and simulation results.

II Dual Fluid Reactor technology

The Dual Fluid Reactor (DFR) is a novel high-temperature, fast reactor concept[1]. It utilizes liquid fuel similar to the Molten-Salt Fast Reactor technology but distinguishes itself by having a core directly cooled by lead. Both circuits can be separately controlled and optimized. This unique characteristic allows for a higher power density compared to other reactors. As a result, the reactor can be more compact and more efficient, reducing both capital and operational costs. This leads to a very high Energy Return on Investment (EROI) compared to other energy sources[2], [3].

The reactor's design is somewhat of a hybrid between Molten-Salt Fast Reactor and lead-cooled reactor technologies, as shown in Figure 1. It combines the advantages of both, offering operational safety, passive safety features, and additional capabilities. One such capability is the absence of high pressure, common in reactors, especially Pressurized Water Reactors, which further reduces costs. Moreover, its hard neutron spectrum and high conversion ratio enable fuel breeding, for instance, U^{233} from thorium, and it is proliferation resistant. It also allows for the reuse of spent fuel from other reactors while significantly reducing long-lived transuranic due to the relatively increased fission cross-section of U^{238} [4], [5]. Therefore, the reactor can achieve high fuel burnup and exceptionally long operation times, even without refuelling, while reducing waste and potentially decreasing existing waste [6]. The high temperature qualifies it as a Generation IV very high-temperature reactor [7]. Besides increased efficiency, this allows for steam production for industrial processes, cogeneration heat, and efficient hydrogen production. However, it also presents challenges for the construction materials. Currently, two types of DFRs are under consideration: one that uses fuel based on molten salts [8] and another, DFRm, which uses metallic eutectic fuel with chromium [4]. This work focuses on the latter. Both types feature high negative temperature feedback, enabling power control solely through this phenomenon. Furthermore, the reactor could theoretically operate without moving parts in the circuits, increasing its lifespan. However, for safety reasons and legal requirements, more conventional control methods like soluble poisons and control rods may be employed. The design is also scalable, meaning both large units and Small Modular Reactors could be developed [9].

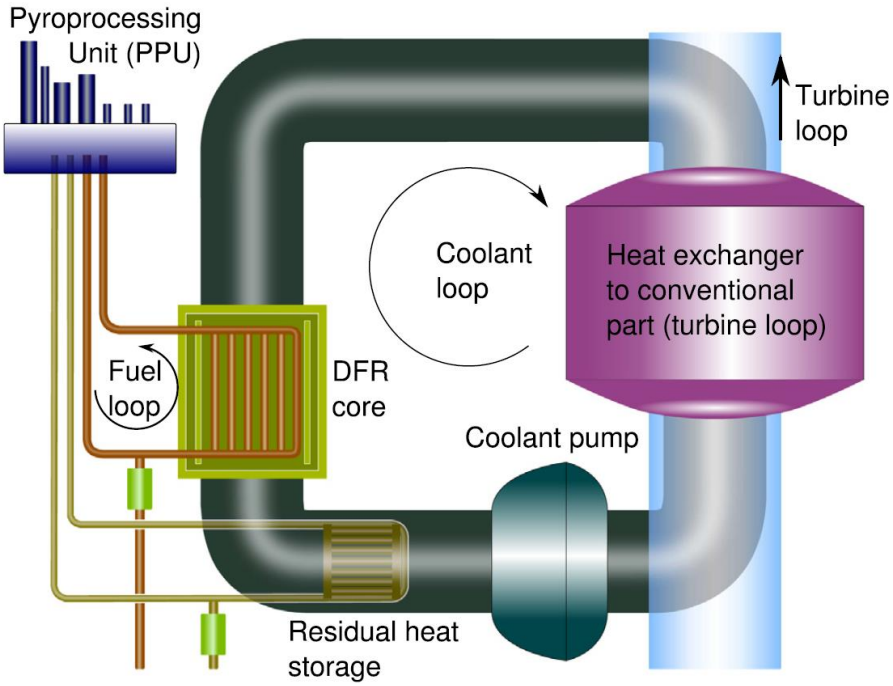

Figure 1: DFR fuel and cooling loop layout by [2]

2.1 Concept Overview

As mentioned, the reactor consists of two loops: the primary fuel loop with eutectic mixture and the secondary coolant loop with lead. The core includes an inlet zone located at the bottom that ensures even distribution and flow of fuel through appropriately configured partitions. This fuel then flows into hexagonally arranged fuel tubes, whose number varies depending on the configuration, before reaching the outlet zone. The core is surrounded by a neutron reflector made of lead, the same material used for the coolant, which also serves as a radiation shield. If included a zone for breeding new fuel is adjacent to this layer. Due to temperature differences in the fuel, natural convection occurs. The flow rate does not need to be high, making this driving force sufficient [10], [11]. However, additional drive pumps can be installed if needed. For safety reasons, it is essential to have a mechanism for the reactor's quick shutdown. In this design, a Melting Fuse at the lowest point of the loop serves this purpose. This is both an active and passive safety feature: in case of increased temperature or loss of power (as the fuse is constantly cooled), the plug melts, leading to a rapid draining of the core and a safe shutdown. In such cases, the fuel flows into tanks below, which are small enough and spaced far enough apart to ensure sub-criticality under all conditions. The use of

liquid fuel eliminates the pressure resulting from fuel swelling; both liquids are at the same pressure, reducing stress. However, the fluid flow will induce vibrations in reactor channels.

The operation of the coolant loop is straightforward: coolant enters the core through tubes in the inlet zone, flows around the fuel tubes, picking up heat, and exits through tubes in the outlet zone. It then moves to a heat exchanger where it transfers energy, cooling down, which can be used for electricity generation, heat, or hydrogen production. A magnetohydrodynamic pump [12], [13] drives the coolant flow, featuring no moving parts, reducing wear and tear, and extending component life. The diameter of this loop's channels is intentionally increased to reduce flow speed and its erosive impact on the walls.

The Pyrochemical Processing Unit [14], [15] enables control of fuel composition, by the online removal of decay products and the addition of new fuel [16]-[18]. This method utilizes electrorefining; the fuel is transformed into salt, and, via electrolysis, fuel metals are isolated, with the majority of decay products remaining in the salt. However, this process is not necessary for DFRm operation due to a significant excess of reactivity [1].

It facilitates the extraction of medical isotopes, it is also possible to continually remove reactor poisons, especially gaseous Xenon, which improves neutron economy. This innovative approach presents numerous possibilities but also poses unprecedented challenges, making further tests essential. Currently used Plutonium and Uranium Recovery by Extraction (PUREX) methods [19] methods require the development of additional infrastructure with enhanced radiation protections, as well as more chemically intensive processes.

2.2 Structural material

Silicon Carbide (SiC) is selected as the construction material for the future Dual Fluid Reactor due to its numerous beneficial properties, even under extreme conditions. These include high hardness and endurance, thermal conductivity, resistance to abrasion, spalling, and creep, low thermal expansion, and resistance to thermal shock. Moreover, SiC shows high radiation resistance, low cross-section for neutron adsorption, and low activation characteristics [20]. It retains its mechanical properties at a proficient level, up to a temperature of 1600°C [21]. It has versatile applications, ranging from heat shields for spacecraft to coating materials and electronics. It is also suitable for solutions in fusion [22], accelerator-driven systems [23], and solar power plants where liquid lead or its alloys are used as coolants. SiC has been successfully used in high-temperature gas reactors as a protective material for TRISO fuel [24], [25], in molten salt reactors as a protective layer for graphite [26], and is even considered for reactors that use water coolant [27]. Broad industrial application results in its availability on the market and thus the possibility of producing the desired shape, as well

as constantly improved production methods give it an additional advantage over other similar robust materials.

SiC occurs in multiple polymorphic forms. The most common are α-SiC with a hexagonal crystal structure, produced at temperatures above 1700°C, and the more robust and desired β-SiC or 3C-SiC with a cubic structure resembling zinc blende [28], it is obtained at lower temperatures. Short bonds of the same length, 1.89Å, in this crystal form contribute to the unique properties of material.

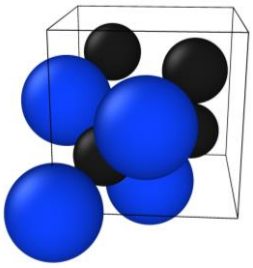

Figure 2: Single crystal cell of 3C-SiC

Compared to other forms under standard conditions [29], it stands out with a higher bulk modulus value of 250 GPa, compared to 220 for α forms, and has a lower thermal expansion of 3.8×10^{-6} K^{-1}. However, its thermal conductivity ($Wcm^{-1}°C^{-1}$) 3.6 is lower than that of others (3.7 for 4H and 4.9 for 6H). It also has the lowest energy gap among polymorphic forms, at 2.36 eV, while for 4H it is 3.23 eV. The density of all crystal types is close to the theoretical value of 3.21 g/cm^3. More accurate data as a function of temperature T (for the crystal from the CVD method) [30] are as follows:

Elastic modulus where E_0 = 460 GPa, B=0.04 GPa/K, T_0=962 K, with Poisson's ratio up to 0.21:

$$E = E_0 - BTe^{\frac{-T_0}{T}}$$

Thermal conductivity ($Wm^{-1}K^{-1}$), it greatly depends on grain size, and is lower for smaller grains but at higher temperatures, this difference becomes smaller [31]:

$$K_p = (-0.0003 + 1.05 \times 10^{-5}T)^{-1}$$

Thermal expansion:

$$\alpha = 2.08 + 4.51\times10^{-3}\,T$$

2.3 Production methods

Advanced production techniques have been developed over the years, each with unique advantages and disadvantages. Particularly interesting are composite materials, such as SiC fibre-reinforced SiC ceramic matrix (SiC_f/SiC) composites, which enhance desirable material properties, including strength and resistance to creep, shock, fatigue, and cracking. Three advanced production

methods are noteworthy: chemical vapour deposition (CVD), chemical vapour infiltration (CVI), and Nano-infiltration and transient eutectic phase (NITE) [30].

The CVD process involves passing vapour phase precursors over a heated material surface, where they react and deposit, forming a high-purity coating [32]. This method uses relatively low temperatures ranging from 900 to 1200°C compared to other methods, reducing mechanical stress and the risk of material damage. Reduced pressure around several kPa is also used to ensure that surface reactions, rather than gas mass transport, control the process rate, minimizing the risk of inhomogeneous mixture formation [33].

The commercially utilized CVI process maintains isothermal-isobaric conditions and is a subtype of CVD. It involves infiltrating a porous material with a mixture of precursor gases that fill the gaps through progressive reactions. The material thus supplied can make up to 70% of the volume fraction; however, it is advantageous to lower this value as the fibres primarily contribute to the composite's strength. A suitably prepared material, known as a preform, with interwoven SiC fibres, for example, in a plane-wave arrangement, is placed in a reactor at temperatures and pressures similar to those in CVD. Precursor gases diffuse into the pores, decompose, and the material is deposited on the surface. Optimal filling is achieved at a temperature of 1320K and a pressure of 3kPa, which unfortunately increases production time and cost [34]. There are modifications to this process aimed at speeding it up, such as forced flow, specialized heating methods like microwaves, and temperature and pressure gradients that can reach up to 1600°C and atmospheric pressure. However, due to control issues and unwanted side effects like higher porosity [35], these are not widely used. Excessive parameters can lead to a situation where external pores are closed, resulting in incomplete densification.

In both of these processes, a mixture of methyltrichlorosilane (CH_3SiCl_3) and hydrogen is used as the precursor gases, allowing for the production of high-purity 3C-SiC. The deposition process is indirect and proceeds via two parallel reactions, gas decomposition and SiC deposition. These gases are advantageous for several reasons: the ratio of deposited atoms remains the same, the produced HCl minimizes the chances of Si crystal formation, and hydrogen improves direct deposition by affecting intermediate compound bonds [36]. In practice, to achieve better parameters, both CVI and CVD methods are used: first CVI to fill the gaps, and then CVD to finish the external layer and protect exposed sections. The material produced in this manner is characterized by good stoichiometry, a density remarkably close to the theoretical one, and exceptionally low porosity. In this way, even a monocrystal can be obtained. The durability of the final product largely depends on the fibres used, with Hi-Nicalon type S of high purity and stoichiometry being the most promising [37]-[39], as confirmed in the corrosion test [40].

The NITE process differs significantly from the previous ones. It relies on liquid phase sintering. Prepared fibres are placed in a slurry containing SiC nano powder with additives like Al_2O_3 or Y_2O_3. The liquid infiltrates the structure, which is then removed and left to dry. The material undergoes hot isostatic pressing at high temperatures, around 1800°C, and pressures reaching up to 20 MPa. This results in a density close to the theoretical one, the process is faster and less expensive. Although the final material shows good thermal properties, it contains trace contaminants from the process and is characterized by a low strain-to-failure ratio, making it more susceptible to damage [30].

2.4 Coolant

To effectively fulfil its function of heat removal, a coolant should possess high thermal capacity, high thermal conductivity, and low viscosity. It should also be minimally chemically active to mitigate corrosion effects. Beyond these fundamental criteria, economic feasibility is also an important factor in consideration. In the context of use in the nuclear reactor, interactions with radiation, particularly with neutrons, must also be considered, as they have a significant impact on reactor performance [41]. The selection of an appropriate coolant involves a trade-off and compromise among these properties. In the nuclear industry, various substances, such as light and heavy water, sodium, lead, and gases such as helium and carbon dioxide, are used. To achieve desired reactor parameters, such as relatively compact dimensions and high-power density, lead stands out as the most suitable candidate for a coolant material.[4], [42], [43]. It satisfies all the criteria, it does not react violently with either air or water, unlike other coolants, such as sodium [12], making its usage and maintenance considerably easier and safer. It does not require additional loops or complex safety measures, and in case of leakage, it solidifies without undergoing any violent reactions. Moreover, it boils at a high temperature of 1747°C, offering a wide operating temperature range without the risks of solidification and boiling. Lead has a lower heat capacity compared to other coolants used in reactors [44], with a specific heat capacity given by (J/kgK):

$$C_p = 156 - 0.0144T \quad \text{at } T \leq 1\,300\ \text{K}$$

However, it compensates for this with a high density, given by (kg/m³):

$$\rho = 11441 \times 12795T$$

It can operate at atmospheric pressure, further reducing the need for additional equipment. From the perspective of interaction with radiation, this stable element also holds advantages over others. It has a low neutron capture cross-section, but a relatively high scattering cross-section, thereby improving neutron economy. Due to its high density, in addition to acting as a reflector, it serves well as a radiation protection, especially against penetrating gamma radiation. Furthermore, short-lived

products formed because of activation, decay back into stable isotopes of lead, ensuring that the chemical composition of the coolant remains nearly unchanged in this context.

2.5 Metallic fuel

Pure uranium melts at a temperature of 1132°C, which is impractical for reactor use. Therefore, a decision was made to utilize an alloy—a eutectic with chromium. The use of such a mixture ensures a lower melting temperature, specifically 860°C [45], lower than that of other suitable metals [46], [47]. This facilitates easier fuel preparation for operations. The eutectic consists of 4.78% chromium and 95.22% uranium by weight, with a proposed enrichment level of 12.8%. It possesses desirable physical properties, such as high thermal conductivity (30.54 W/mK) and provides a high actinide concentration. This results in a better neutron economy due to reduced moderation and lower adsorption, thereby enhancing performance and enabling economically favourable lower enrichment [5]. Liquid uranium has the highest viscosity compared to other elemental metals, and the small addition of Cr does not significantly affect this property. At 1150°C, liquid uranium has density of 17.24 g/cm^3, as compared to nearly eutectic composition, 15.91g/cm^3[48]. Where the density of uranium is given by the equation (g/cm^3):

$$\rho = 19.083 - 16.01 \times 10^{-4} T$$

and the equation that takes into account the interaction with chromium [49]:

$$\rho_{U-Cr} = 0.985 \left(\frac{100}{\frac{wt\%Cr}{\rho_{Cr}} + \frac{wt\%U}{\rho_U}} \right)$$

III Corrosion

Corrosion of ceramic materials by liquid metal is a complex phenomenon that occurs through various mechanisms simultaneously and varying depending on the location within a single closed loop. When considering chemical interactions, reactions occur at the interface, either directly with the medium or with contaminants. The resulting products can be in any state of matter or their combinations. Gaseous products are generally volatile; hence, their removal significantly affects reaction equilibrium, potentially leading to accelerated degradation, mass loss, and consequently increased porosity. In the case of liquid phases, similar effects can be observed, especially when the medium is in motion. Solid reaction products may form a protective layer that shields the material from further corrosion and may even improve its mechanical properties. However, in many cases, excessively rapid formation of oxides, on the surface results in the creation of scales, which may detach and be carried away by the flow. On the other hand, if the process is too slow, the resulting layer does not fully cover the surface thus failing to provide proper protection.

It is crucial especially when dealing with liquid metals to ensure stoichiometry of the composition, as excess unbound substances will dissolve in the solution, creating pores, exposing grain boundaries, and significantly increasing the exposed surface. In general, it can be assumed that *the more compact or tightly bonded materials corrode less whether they are glasses or crystalline materials [50].* Therefore, a production method that ensures a smooth surface, with the high chemical purity and low porosity is crucial.

3.1 Corrosion mechanisms

Corrosion in flowing metals emerges from a variety of mechanisms that are often interconnected. Some of these effects result exclusively from the interactions between metal and ceramics at high temperatures. These include: the dissolution of material in the liquid, intensified by temperature; mutual reactions between substances or reactions with impurities, especially oxygen; the diffusion of metals into the material, and additional mass transport induced by the presence of a temperature gradient. The flow of metal amplifies these effects as it continually introduces fresh material and removes by-products from ongoing reactions. This process also influences the increase in temperature gradient and exerts an erosive action, damaging protective layers and removing material layers. As a result, the surface area exposed to corrosion increases [51]. Given that the coolant will move much faster than the fuel, those effects may be more pronounced, despite its lower temperature. Therefore, further analysis primarily focuses on the coolant. At lower velocities, equilibrium is established, with the dissolution process is controlled by diffusion in the boundary

layer of the liquid. As velocity increases, the diffusion rate grows until the interfacial reaction rate becomes the controlling mechanism, at which point the corrosion rate becomes independent of it. However, at higher velocities, erosive corrosion can occur, damaging the protective layer and potentially stripping away layers of material. Additionally, due to the high density of the metal, cavitation may also occur [52].

Within the loops, both temperature and flow rates will vary, with peak values occurring at the reactor core. Due to the temperature-dependent solubility, mass transport will occur from warmer to cooler areas. Even though solubility in lead is low, for carbon estimated to be 0.014 wt% [53] and 0.029 wt% for silicon [54], [55] at 1000°C, it must be considered, especially when long non-stop use is intended. This is crucial to consider, as it may result in flow restriction and even clogging of heat exchanger narrow channels [50].

Flow within pipes also induces vibrations, which due to material fatigue can lead to the formation of micro-cracks, thereby intensifying corrosion. Similarly, temperature fluctuations also contribute to this effect but due to the low expansion factor to a lesser extent. This issue becomes particularly significant in the case of tubes with small diameters and potentially thin walls. These cracks can localize, accelerating material degradation through increased corrosion [56].

Radiation in a reactor also contributes to material corrosion. When high-energy neutrons or ions collide with lattice atoms, they cause displacement, resulting in the formation of dislocations and vacancies. Often, this process is accompanied by the cascade effect, which intensifies these effects and leads to the formation of micro-damage [57]. In this context, high temperature is beneficial as it leads to a reduction of these effects through thermal annealing [58]. From a macroscopic perspective, radiation leads to material swelling [59], resulting in increased fibre-bridging stresses. Consequently, initial crack velocities are faster, but the growth rate decrease with higher doses. The absorption of neutrons results in element transmutation, thereby changing the composition and chemical potential of the material [28], [60], [61].

3.2 Corrosion by lead

To validate the use of materials in the reactor, high-temperature tests are essential, especially considering the long-term operation of the reactor without fuel replacement. In short-term studies, material losses or deposits may fall within the range of measurement error yet become significant over an extended period. This discrepancy is crucial, as the materials' long-term performance under high-temperature conditions can significantly differ from the short-term test results. Issues such as slow crack growth, creep [62], and long-term oxidation or corrosion are often not apparent in short-term tests. Therefore, conducting dedicated tests to examine the reactor's long-term operating

conditions is highly recommended for precise material validation. At moderate temperatures, lead is reported to be inactive with SiC [63], among other factors, not wetting it [64]. The available sources discussing corrosion caused by flowing lead usually are for temperatures lower than those intended in DFR [44]. Tests conducted at the target temperature have been performed on steady-state liquids or alloys, providing only partial information [65]-[68].

A short-term screening study [40] at the target 1000°C temperature provide many interesting conclusions about the mechanisms of this process. High purity, full density composites produced through CVD have shown very promising results in terms of compatibility with pure liquid lead. A sample created via the silicon melt infiltration process experienced increased mass loss due to the dissolution of excess silicon in lead, highlighting the crucial role of stoichiometry in the crystal structure. This process results in pit formation and an increased proportion of α-SiC, predominantly in the 6H form. This effect can also manifest for carbon, even in proper materials, leading to the formation of an amorphous Si layer on the surface [69]. Lead intrudes into the material through open pores [70] and at grain boundaries, which subsequently leads to bond weakening and embrittlement [71]. Research on the PbLi alloy for the fusion blanket reveals no significant reaction up to 900°C and establishes 1100°C as the maximum safe operating temperature. While pure lithium reacts intensely with silicon carbide, its impact is negligible at low concentrations. Therefore, this value should also be considered the maximum permissible for pure lead [72]-[74].

3.3 Oxidation and influence of oxide layer

Silicon carbide, a non-oxide material, tends to oxidize in the presence of oxygen, although the rate of these reactions is low. Under appropriate conditions, a thin passivation layer forms, which protects the material and slows further oxidation. As a result, this process has undergone extensive investigation through both theoretical and experimental research. These studies have demonstrated that oxidation follows a parabolic rate law, indicating that diffusion is the controlling mechanism. Depending on temperature and oxygen concentration, the process may proceed via either a desirable passive oxidation or an active oxidation [75]-[78]. In passive oxidation, silica forms through reactions with dissolved oxygen and deposits on the surface, creating a dense layer. Oxygen can diffuse through this layer in both molecular and ionic forms. The latter is more energetically demanding, requiring the breaking of bonds, and thus becomes significant at considerably higher temperatures, above 1300°C [79], [80]. The concurrent effects of these two diffusion channels can lead to a significant acceleration of corrosion. Even a brief exceedance of this temperature can have significant effects, as SiC will start to react directly with the silica layer, generating gaseous products that increase pressure between them, which can lead to cracking of the protective layer [75]. The C-terminated surface exhibits higher activity, and as a result, its degradation proceeds up to an order of magnitude faster

[81], [82]. The exact values vary depending on the composition of the material, hence, on the production method; therefore, detailed testing is recommended. Excessively high oxygen concentrations can also lead to increased corrosion due to the excessive growth and cracking of the formed Si-enriched layer [83]. Despite relatively low solubility in fuel, 0.005 wt% in liquid uranium [84] and 0.009 wt% in chromium [85], and high for coolant 0.013 wt% [86] to achieve the desired oxygen concentrations, additional purification methods must be implemented to remove its excess from the liquids. Silica is reported to have the lowest oxygen diffusion coefficient among oxides, a critical factor in determining the oxidation rate and the growth of the oxide layer thickness [87]. Additionally, this layer suppresses diffusion of gaseous by-products, leading to an increase in their concentration and thus further slowing down degradation. It has also been reported to be more effective at retaining fission products than SiC [88]. Under reactor operational conditions, the silica layer remains amorphous; however, at higher temperatures, it can transition to a cristobalite crystalline form [89], where oxygen diffusion is even is even further reduced. The emerging layer fills surface gaps, thereby reinforcing the material, and can even rapidly seal matrix cracks. Considering the necessity of gas diffusion into and from pores, these pores will not be completely filled but will instead close at their mouth. At temperatures below 1000°C, the rate of oxide formation slows considerably, potentially leading to degradation of unprotected material fibres. Therefore, pre-oxidizing the construction material is recommended. Cubic SiC, in comparison to other forms such as 4H and 6H, also stands out due to its oxidation rate, which can be up to ten times higher [90]. The thickness of the oxide layer increases in correlation with both temperature and exposure time. It also increases with an increasing flow rate [67], which can be explained by a shift of active-to-passive transition partial pressure for a given temperature towards lower values, due to an increase in non-equilibrium reactions – namely, the supply of oxygen and the removal of reaction products.

The dominant reactions in passive mechanism are as follows [91]:

$$SiC + 4O \rightarrow SiO_2 + CO_2$$

$$SiC + 3O \rightarrow SiO_2 + CO$$

$$SiC + 2O \rightarrow SiO_2 + C$$

Active oxidation results in rapid material degradation and pits formation. The free energy changes for these reactions are smaller, hence, they only become significant at higher temperatures; under the right conditions, this process will dominate at lower partial pressures of oxygen. Reactions most relevant to the active oxidation are as follows:

$$SiC + 3O \rightarrow SiO + CO_2$$

$$SiC + 2O \rightarrow SiO + CO$$

$$SiC + 2O \rightarrow Si + CO_2$$

Change in Gibbs free energy ΔG, as a function of temperature T for these oxides, can be presented as:

$$\Delta G = \Delta H - T\Delta S$$

Where ΔH represents the change in enthalpy, and ΔS represents change in entropy. The combination of these functions, normalized to one mole of oxygen for different reactions, is depicted in an Ellingham diagram, as shown in Figure 3. Silicon dioxide is more stable – has a lower formation energy than chromium oxide. However, it can already be observed at this stage that silica is more stable than gaseous silicon monoxide and carbon monoxide only up to a certain temperature; beyond that, the equilibrium will shift towards the production of SiO. Due to the high stability of uranium oxide, it is a preferred fuel form in reactors [92]. However, this proves to be disadvantageous in the case of liquid fuel, as it requires maintaining a very low partial pressure of oxygen. Under these conditions, a protective layer cannot form within fuel loop.

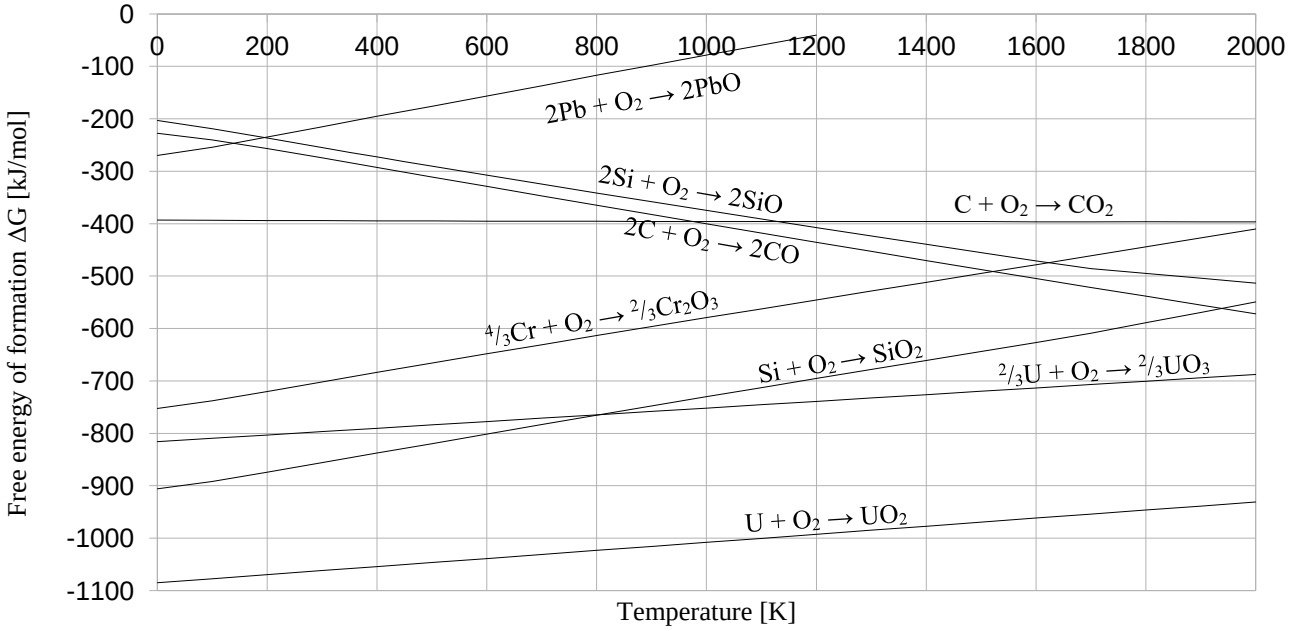

Figure 3: Ellingham diagram of oxides, created based on data from NIST-JANAF database [93]

Subsequently, in order to analyse the dependence on gas concentration, calculations of the standard free energy change of the presented reactions were conducted, employing Hess's law:

$$\Delta G^0_{r,T} = \sum v_p \, \Delta G^0_{f,T}(products) - \sum v_r \, \Delta G^0_{f,T}(reagents)$$

The relationship for chemical equilibrium under non-standard conditions is used:

$$\Delta G_{r,T} = \Delta G^0_{r,T} + RTln\left(\frac{\prod a_p^v}{\prod a_r^k}\right)$$

Where a represents the activity of the reactants r and products p, and v, k are the reaction coefficients. The concentrations of the products were assumed to be unity, and this assumption was used to derive the dependencies presented in Figure 4 bellow.

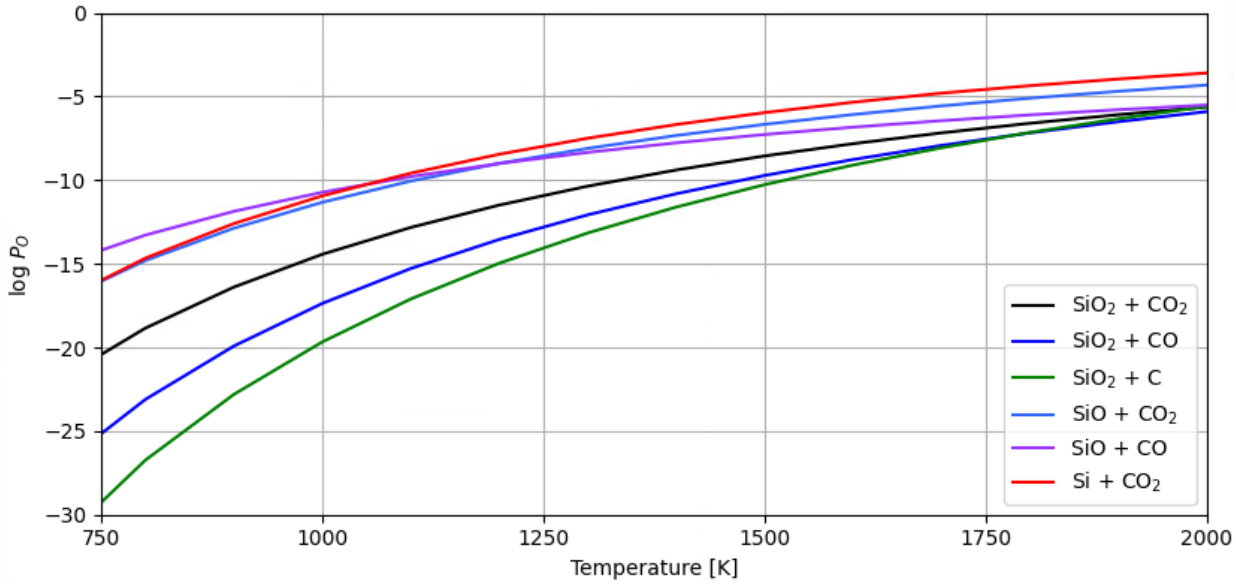

Figure 4: Dependence of the reactions equilibrium on the temperature and the partial pressure of oxygen

At lower temperatures, reactions characteristic of passive oxidation dominates; however, as temperatures increase, the equilibrium shifts, and active oxidation reactions begin to prevail. The state of the system is strongly influenced by the concentration of the reaction products. As the concentrations of the reaction products decrease, unfavourable reactions begin to dominate at lower temperatures and lower partial pressures of oxygen. At low concentrations of 10^{-7}, which might occur due to the removal of material from a clean surface by metal flow, for a temperature of 1100°C, active oxidation can occur even at an oxygen partial pressure of 10^{-20}. When the oxygen concentration is higher, passive oxidation resumes, as detailed in the study [94].

3.4 Interactions with uranium and chromium

Silicon carbide is used as a protective layer in TRISO fuel, where it serves not only as mechanical protection but also as an effective barrier that slow down the diffusion of fission products [57], [95]. In addition to its extensive list of applications, it is also employed as a crucible for melting metals [96]. As a semiconductor, this type of crucible can be heated with microwaves, enabling enhanced system isolation. Additionally, SiC is one of the few known ceramics to maintain

microwave susceptibility at temperatures exceeding the melting temperature of pure uranium [97], [98]. As indicated earlier, the high stability of uranium oxide means that equilibrium is reached at low oxygen partial pressures; thus, a protective silica layer cannot form. The exposed surface will be susceptible to dissolution corrosion [99], but the low velocity of the fuel effectively limits mass transport and erosion. According to the phase diagrams, carbon and silicon will dissolve in liquid uranium [100]. The transition of carbon into the solution, particularly at higher concentrations in colder regions, will result in the precipitation of solid particles.

As demonstrated in Figure 5 at reactor operating temperatures, chromium carbides are more stable than silicon carbide, the same is true for silicides. During the interaction with pure chromium, a layered structure forms, with silicides dominating at the SiC surface [101]. As demonstrated by the study [102], these silicides can penetrate the material's structure and bind the grains, enhancing durability. The outer layers of chromium carbide exhibit different thermal expansion characteristics. Consequently, temperature fluctuations and the resultant stresses are likely to cause cracking, and scales will be carried away by the metal flow. This layer does not minimize diffusion as effectively as SiO_2, resulting in the continuous release of carbon from the material. At the core's hottest point, dissolution will be particularly intense, posing a threat to the integrity of the tubes; for this reason, applying an additional coating in this area is advisable. Suitable materials may include the ceramic Y_2O_3, a Mo layer with high corrosion resistance [103], [104], or other carbides such as TiC [105] or ZrC [106], [107].

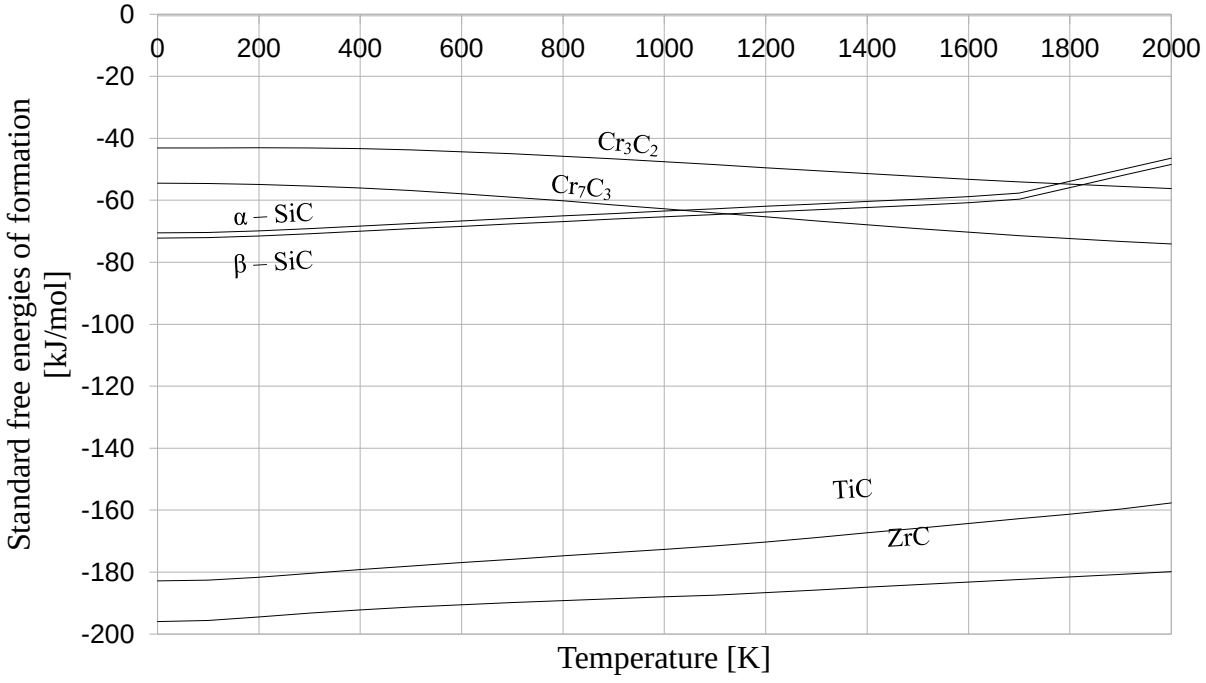

Figure 5: Ellingham diagram of carbides created based on data from NIST-JANAF database [93]

3.5 Interactions with other impurities

Using materials in a system that could react with each other is not recommended, even in the absence of direct contact, because mass transfer can occur via the fluid due to concentration differences. Studies show that there are undesirable interactions between steel and SiC [108]. The effect is significant even at a temperature of 700°C, where there is a reaction between Fe and Cr lead to the formation of carbides and silicides of these metals. This results in a mass gain by SiC and an increased mass loss of those alloys [109]. Similarly, negative interactions will occur with titanium-zirconium-molybdenum alloy – a proposed construction material – as elements entering the solution will interact with it and cause the formation of layers of carbides and silicides [78]. This is also crucial regarding the need to control oxygen concentration, which will differ for each material. For this reason, to minimize the use of other materials, electrodes made of a different type of SiC composite with lower resistivity, such as those with a higher carbon content, can be used in the magnetohydrodynamic pump [110]. The temperature in the pump will be lower, mitigating the effects of corrosion.

3.6 Limitation of corrosion effects

To mitigate the effects of corrosion, it is essential to conduct regular inspections of the fuel and coolant quality, clean the circuits to remove accumulating sediments, it is also important to implement appropriate preparatory measures, and limit the operating parameters of the reactor. The most crucial aspect is selecting the proper method of producing the composite structure, with the CVD followed by CVI method being the most suitable. This method ensures a dense, stoichiometric coating without pores, guaranteeing excellent resistance. The C-terminated crystal side is more active and susceptible to dissolution and oxidation; therefore, if possible, a crystal Si-terminated should be applied.

Furthermore, minimizing the involvement of other active structural materials in contact with fluids is essential to avoid undesirable inter-material reactions. For the cooling loop, corrosion mitigation strategies include limiting the temperature to 1100°C, pre-oxidizing the entire loop to create a passive oxide layer, and optionally annealing it to achieve a more resistant crystalline form. Additionally, actively controlling and maintaining the oxygen concentration at an appropriately high level is crucial to sustain passive oxidation and prevent active oxidation. However, it should not be too high, as an excessively thick layer may lead to flaking. The precise values of these parameters depend heavily on the reactor's specifications, particularly its maximum temperature and flow rate.

The situation is more complex for the fuel loop, as it requires maintaining the oxygen concentration at the lowest possible level. Under these conditions, dissolution corrosion will be the prevailing issue. To mitigate this effect, it is necessary to consider appropriate doping of the material to reduce the charge of the emerging carbon vacancies and to adjust the Fermi level adequately [111]. As previously mentioned, the interaction between chromium and SiC resulting in silicide compounds can enhance the surface condition. This property can be utilized by exposing the wall materials to chromium at high temperatures during the preparatory phase. However, this approach will be insufficient at the highest temperatures. Therefore, the use of appropriate protective coatings of Y_2O_3, or Mo is advisable, at least in the core. An additional option is the intentional addition of carbon to saturate the solution, thereby limiting its escape from the material [40].

IV Simulations

Corrosion is a process that occurs at the interface between different media. Therefore, it is crucial to thoroughly understand the surface structure and the effects of interactions between materials. For this purpose, in addition to experimental and thermodynamic analyses, computer simulations can be utilized. Specifically, Density Functional Theory (DFT) simulations and Molecular Dynamics (MD) simulations facilitate a more in-depth analysis of structural and electronic states. Due to their computational complexity and significant computational power requirements, these simulations can only determine nanoscale, short-term effects in feasible computation time. Nevertheless, they provide enough detail to accurately identify the dominant reaction mechanisms and determine specific characteristic variables that may be vital for long-term corrosion studies. All calculations were performed on the Świerk Computer Centre – CIŚ computational cluster located at National Centre of Nuclear Research.

4.1 Density Functional Theory calculations

Density Functional Theory plays a crucial role in quantum mechanics modelling, finding extensive application in materials science and condensed matter physics. It provides a practical balance, offering computational accuracy while maintaining feasibility, positioned between the highly accurate but computationally intensive methods of quantum mechanics, and simpler empirical approaches. The foundation of DFT lies in the two Hohenberg-Kohn theorems. The first states that the electron density in the ground state of a multi-particle system uniquely determine the electric potential acting on all electrons, meaning the system's energy can be described by single variable – electron density, which is a function of coordinates. The second theorem asserts that any alteration in the electron density of a system will result in states of higher energy than the ground state [112]. Thus, by systematically varying the electron density, it is possible to approximate the minimum energy corresponding to the ground state. Subsequent modifications by Kohn and Sham involving the decomposition of the many-body problem into a system of non-interacting single electrons, enabled a practical solution to the problem. For these particles, the Schrödinger-like wavefunction equations are solved, incorporating an exchange-correlation correction term to better approximate interactions represented by full configuration wavefunctions [113]. To address this issue, various approximations have been developed, including the Local Density Approximation (LDA), the Generalized Gradient Approximation (GGA), hybrid with Hartree-Fock method and others [114].

4.2 Methodology

Using the described methods, a study of lead adsorption on 3C-SiC was conducted. For calculations, the open-source software package Quantum Espresso was utilized, which supports a broad spectrum of exchange-correlation functionals and boasts an extensive database of pseudopotentials. The modular structure of this software allows for the study of various physical and chemical properties. Its primary method involves simulations using the self-consistent field (SCF) approach with the aim of iteratively converging the ground state of the system to a predetermined threshold value.

The pseudopotentials employed are based on the Projector Augmented-Wave (PAW) method. This technique uses projectors to implicitly incorporate the effects of core electrons, substituting them with appropriately corrected pseudo-wavefunctions, making calculations more efficient. The electron exchange-correlation effects were addressed within the Perdew-Burke-Ernzerhof (PBE) exchange-correlation functional which is specific form of GGA. This functional is a modification of LDA, it incorporates not only the density of electron states but also their gradient in calculations. As a result, GGA can provide a more detailed representation, proving especially useful for systems with rapidly varying electron densities, such as crystal surfaces or molecules. The choice of method was motivated by its adoption by other researchers in similar research topics [111], [115], [116]. Unfortunately, this method does not reflect the energy gap well, underestimating it. Energy cut-offs were used for the wavefunctions and the charge density that exceeded the minimum recommended values of the employed pseudopotentials and were set to 680 eV and 4762 eV, respectively. Convergence tests conducted on smaller cells validated this choice. Lead is a heavy metal, therefore, relativistic effects become significant and influence its electronic properties. Pseudopotentials that incorporate relativistic corrections were selected. To account for spin-orbit coupling effects, the calculations were conducted using non-collinear spin polarization. The initial step involved determining the lattice parameter based on the unit cell. By integrating the Birch–Murnaghan isothermal equation of state over pressure, an equation in which the energy of the system is dependent on the volume is derived.

$$E(V) = E_0 + \frac{9V_0K}{16}\left\{K'\left[\left(\frac{V_0}{V}\right)^{\frac{2}{3}}-1\right]^3 + \left[\left(\frac{V_0}{V}\right)^{\frac{2}{3}}-1\right]^2\left[6-4\left(\frac{V_0}{V}\right)^{\frac{2}{3}}\right]\right\}$$

Where V represents volume and K denotes bulk modulus. Minimal volume can be derived by fitting the curve to the results obtained for varying cell volumes. The acquired lattice constant (4.379Å) aligns with the simulation [117] and the experimental results [118] (4.348Å), which was used to create the adsorption models with Vesta software [119]. The acquired bulk modulus yielded a value of 222

GPa compared to 230 GPa, which is close to the expected value for this exchange correlation functional [120].

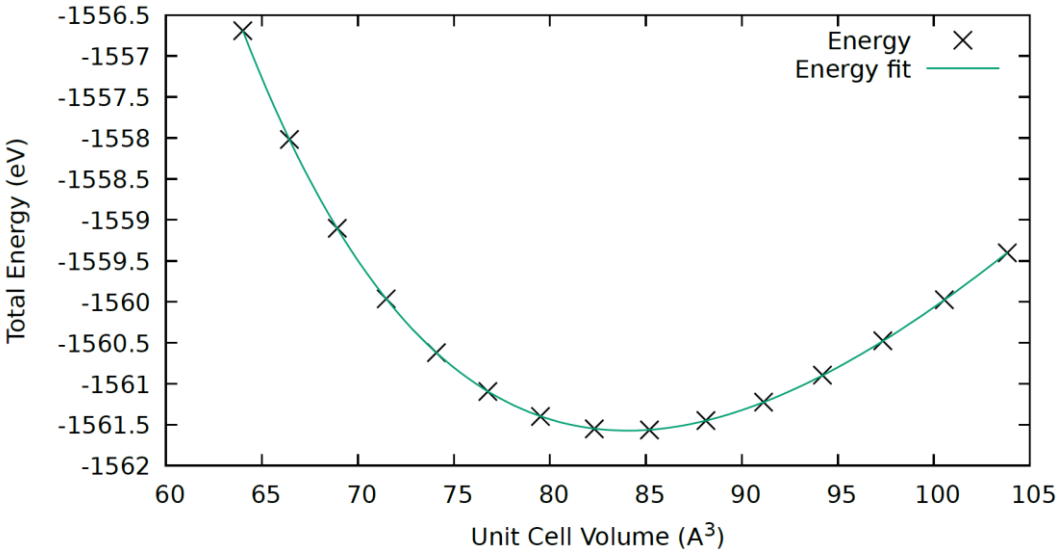

Figure 6: Fitting of Birch–Murnaghan isothermal equation to change of total energy in function of volume.

In subsequent simulations, supercells were utilized, created by dividing the crystal along three representative low-index crystal planes (100, 110, 111). Such a setup necessitating certain computational adjustments. Since the computational box still has periodic boundaries, the computational space is equivalent to a very thin slab. It is essential to use a sufficiently large vacuum gap to limit interactions with the image of the next slab, in this case three lattice constants in the z-direction were employed. In such a system, symmetry is maintained in two dimensions, which should be taken into account for band gap calculations, indicating that the benefits of system's periodicity cannot be harnessed. Such a slab has two surfaces, hence, to avoid undesired interactions and better represent the surface state, bonds on the underside are saturated with hydrogen atoms. It is advantageous to use state smearing to facilitate convergence and avoid numerical issues, ensuring the value remains small to prevent introducing significant changes.

The relaxation process is also iterative; for each supercell configuration, SCF calculations are performed, and subsequently, the forces acting on the atoms are computed based on these calculations. Following the Broyden-Fletcher-Goldfarb-Shanno (BFGS) method, atom positions are updated based on quasi-Newtonian equations. This procedure is repeated until convergence is reached, meaning when the forces acting on the atoms fall below a set limit of 0.02eV/Å and total energy changes are below 0.13 meV. A mixing factor, crucial for updating the electron density between SCF iterations, was set at 0.3. During relaxation, atomic positions are altered in up to the three topmost layers, while the atoms of the two lowermost layers and the hydrogen layer are immobilized, mimicking their positions in the bulk crystal. Given the significantly higher computational power requirements and

the fact that high accuracy in the states density is not as crucial when determining the system atoms lowest energy positions, certain parameters can be reduced relative to the target calculations, such as the electron convergence threshold and the number of K-point sampling of the Brillouin zone. In the relaxation calculations, K-point grid of 6×6×1 was utilized, and convergence threshold was established at 10^{-6} eV while for the target SCF calculations for relaxed systems employed a 10×10×1 Monkhorst-Pack mesh and a threshold of 10^{-7} eV. This method allows for the determination of the transferred charge by conducting a Bader charge analysis and calculating the charge density difference (CDD). The latter illustrates the disparity between the charge density of a system and a reference configuration without the adatom, and lead atom itself. The adsorption energy E_{Ad} can be determined using the given equation:

$$E_{Ad} = \frac{E_{SiC+Pb} - E_{SiC} - NE_{Pb}}{N}$$

where E_{SiC+Pb} represents the total energy of the entire system, E_{SiC} is the energy of the clean slab, E_{Pb} is the energy of an isolated lead atom and N denotes the number of adatoms.

On the surfaces of crystals formed by cutting through the bulk crystal along specific planes, unbalanced forces emerge. Hence, before proceeding with the target simulations, it is essential first to relax these surfaces [121]. Adsorption simulations were prepared by placing lead atoms on such reconstructed samples at characteristic high-symmetry points. For the (100) surface, these positions include T (on top), B (bridge), SB (short bridge), LB (long bridge), and H (hollow), as shown in the Figure 7. For the (110) surface, positions T and B were also examined, as well as two hollow positions: HC, which is closest to two carbon atoms from the top row, and analogically HSi, close to silicon atoms, as indicated in Figure 9. For (111), both T and B were examined along with two hollow positions; specifically, the face-cantered cubic located between three atoms and above a lower-row atom and the hexagonal close-packed above an empty space, as illustrated in Figure 11.

In the study, different coverages were considered, represented as the fraction of monolayer (ML) coverage. The smallest values of 1/9 and 1/16, involved placing a single adatom on a surface composed of 3×3 and 4×4 unit cells, respectively. Subsequent configurations involved placing one or more atoms on a 2×2 surface. Incorporating multiple adatoms within a single simulation box enables a more detailed examination of Pb-Pb interactions, which is particularly relevant for larger coverages.

The subsequent step involved conducting non-self-consistent field (NSCF) calculations, which provide a more detailed insight into the electronic properties of the system, enabling the investigation of the band structure and the density of states. While SCF aims to achieve convergence of the electron density in the ground state, NSCF calculations take these results and focus on a detailed exploration of the electronic structure, such as density of states and band structures. To accomplish

this, enhancing the density of K-points is crucial, and a 25×25×10 mesh was employed, alongside considering a greater number of bands accounting for both occupied and unoccupied states, which is particularly important in calculations including non-collinear spin polarization.

4. 3 Results

(100) Surface

The (100) surface of the cubic crystal is polar and exhibits a fourfold rotational symmetry. It typically forms dimers in a linear 2×1 reconstruction or other more complex configurations found in larger samples [122]. Therefore, in this case, this arrangement was treated as the base unit for creating the grid, as shown in Figure 7. To maintain periodicity, the lowest coverage studied for this surface was 1/16, rather than 1/9 as in other cases. The surface reconstruction, terminated by carbon atoms, was successful, with the resulting C-C bond length of 1.374 Å closely aligning with research findings (1.36 Å) [123].

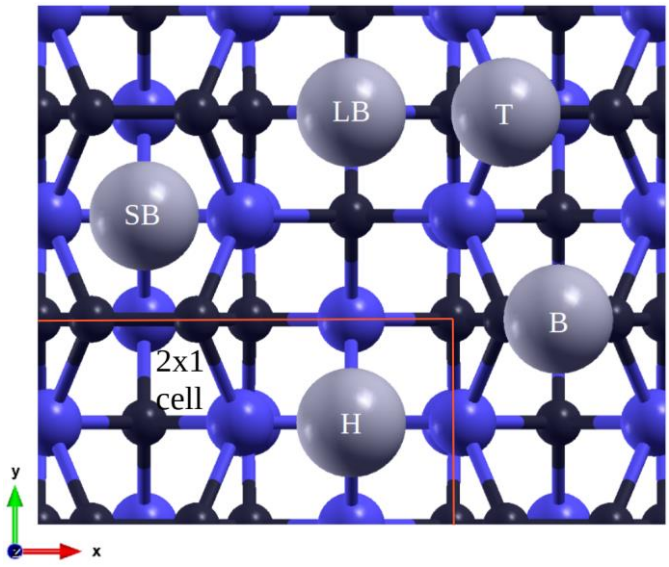

Figure 7: Initial sites of Pb (grey) on SiC (100) surface, Si (blue), C (black): LB long bridge, T on-top, SB short bridge, B bridge, H hollow. This colour designation will be used in the remaining figures.

For this configuration, the on-top position proved to be unstable for all coverages. The obtained results are presented in Table 1. At lower coverages, the short bridge position is the most stable, with bond lengths of 2.47 Å. As the coverage increased, resulting in denser packing, the long bridge and bridge positions became more stable. However, they do not precisely match their positions from lower coverages, forming bonds with lengths of 2.35 and 2.43 Å. At a 3/4 ML coverage, a second layer of lead atoms was formed.

Adsorption sites	1/16 ML	1/4 ML	1/2 ML	3/4 ML
Short bridge (SB)	-2.33	-2.15		
Charge transfer form lead	0.89	0.76		
Long bridge (LB)	-2.09	-2.16	-2.16	-2.04
	0.73	0.66		
Bridge (B)	-1.92	-1.83	-2.16	-2.04
	0.84	0.68		
Hollow (H)	-2.05	-2.23		
	0.73	0.66		

Table 1: Adsorption energy and lead charge transfer for (100) surface, C-face

During the reconstruction of surface terminated by silicon atoms, the formation of dimers was not achieved, even when atoms were manually positioned in the target locations. In this dimer, the Si-Si bond is weak, making it unstable [124], [125]. Given the small surface energy difference observed with and without dimers is small [124] therefore, this configuration was used in calculations. In this context, the SB position is equivalent to H and LB to B, analogically to structure depicted on Figure 7. In this case, the on-top position demonstrated stability for intermediate coverage, but a significantly lower adsorption energy suggests that it fell into a local minimum. The most stable position is also SB, but a much longer bond is formed here 2.74Å. With higher coverage, due to mutual repulsion, the adatoms shifted to position B. Here, one can observe a lower energy than for a 1/4ML coverage, resulting from occupying the free B position nearby and the displacement of silicon atoms also forming an alternating row. With higher coverage, a second layer of lead atoms was also formed.

Adsorption sites	1/16 ML	1/4 ML	1/2 ML	3/4 ML
Short bridge (SB)	-2.53	-2.19		
Charge transfer form lead	0.32	0.23		
Top (T)		-1.09		
		0.27		
Bridge (B)	-2.23	-1.88	-2.24	-1.83
	0.33	0.2		

Table 2: Adsorption energy and lead charge transfer for (100) surface, Si-face

The following CDD Figure 8, shows that charges mainly accumulate around carbon atoms. In the case of surfaces terminated with Si, they are transferred to deeper layers of the crystal, notice difference in isosurface level.

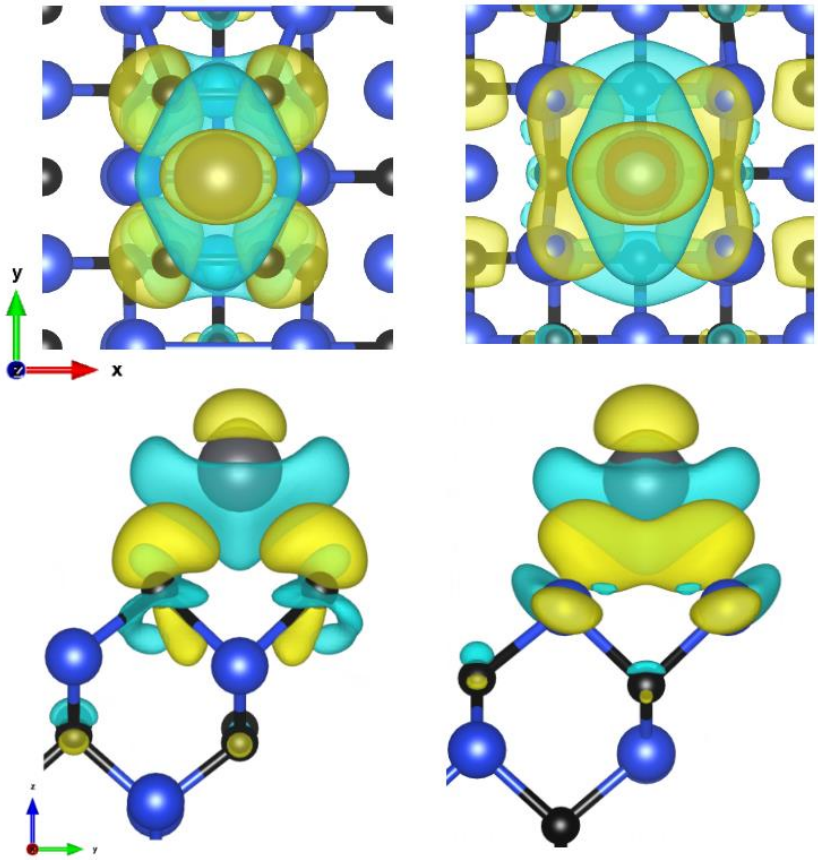

Figure 8: Top and side view of CDD visualization of C-face, left with isosurface of 2.8 me/Å^3 and Si-face, right with 1.9 me/Å^3 of (100) plane 1/4 ML, for both SB adsorption site. The yellow colour represents an increase in charge density, while blue represents a decrease. This colour arrangement will be consistent for the rest of the charts.

(110) Surface

For the (110) crystal surface, there is a double rotational symmetry, Si and C atoms occur in one row, hence it is non-polar. In this case, the T positions for both Si and C are unstable, while the B position was stable only for a 1/8 ML coverage. However, it did not remain in its original position but moved to a new one along the line of carbon atoms in the top row, as depicted in Figure 9, and it has a significantly lower adsorption energy than other positions -1.54 eV. Of the stable configurations, HSi and HC, the latter is more stable for all coverages, with the smallest bond lengths being respectively to the carbon atoms and to the silicon atom. Similarly, in the simulation with two adatoms, they prefer to occupy second nearest neighbouring position from first adatom, and in this way creating alternating rows. Despite low Pb-Pb distance, atoms interact weakly because of screening, and the

energy per atom is lower than for 1/8ML. At higher coverages, further free HC positions are occupied, and energy again rises as shown in Table 3.

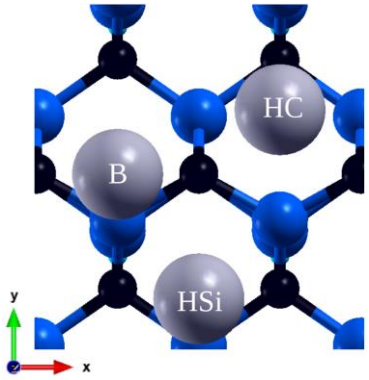

Figure 9: Top view of (110) surface with final relaxation positions, HC nearly above C from bottom row closest to two C atoms from top row, Hsi closest to Si and B above atoms from top row

In this case, even though there is a significant difference in adsorption energy, the transferred charge is similar. On one hand, carbon atoms strongly attract charges towards themselves, and on the other, as can be seen in Figure 10, silicon atoms transfer charges to the next three carbon atoms, thereby reducing bonds strength.

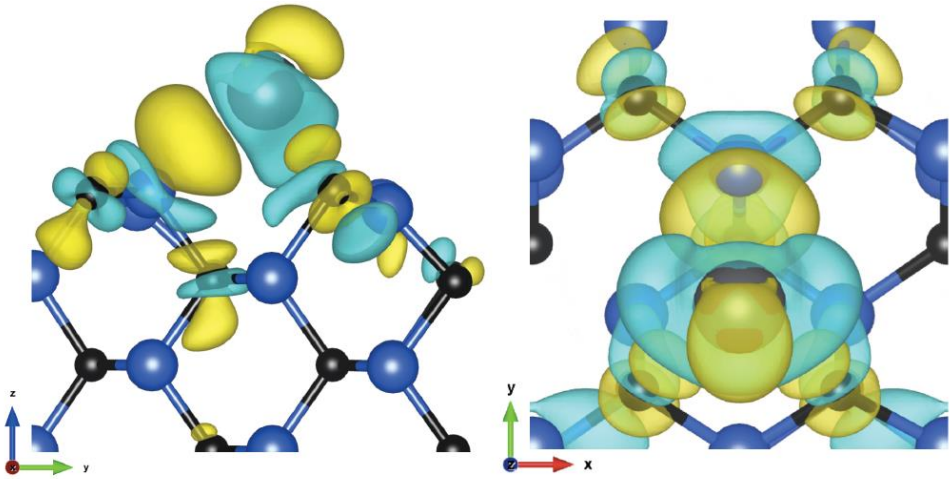

Figure 10: CDD of (110) plane at 1/4 ML HC position, side, and top views (isosurface value: 2.2 me/Å^3).

Adsorption sites	1/18 ML	1/8 ML	1/4 ML	3/8 ML	1/2 ML
Hollow Si (HSi)	-2.05	-1.99			
Charge transfer	0.49	0.45			
Hollow C (HC)	-2.36	-2.34	-2.81	-2.46	-2.34
	0.48	0.46			

Table 3: Adsorption energy and lead charge transfer for (110) surface

(111) Surface

The crystal can be divided by the (111) plane in two ways, resulting in a hexagonal configuration with either one or three dangling bonds per atom on the surface, the first case was examined. Such a surface has a sixfold rotational symmetry. Unlike the previous ones, a hexagonal simulation box was used here, proving crucial for the proper surface reconstruction. Due to its high symmetry, only vertical displacement was observed during this process. In both cases, for a 1/2ML coverage, the adatoms settled in a honeycomb grid, occupying the on-top and hpc positions, and for higher coverages, a hexagonal grid was formed where all three studied positions were occupied, as shown on Figure 11. For the C-terminated surface, the distances between lead atoms were 3.52 Å and 3.55 Å, respectively. For the Si-terminated surface, the hexagonal configuration is less regular, with distances of 3.56 Å and an average of 3.57 Å.

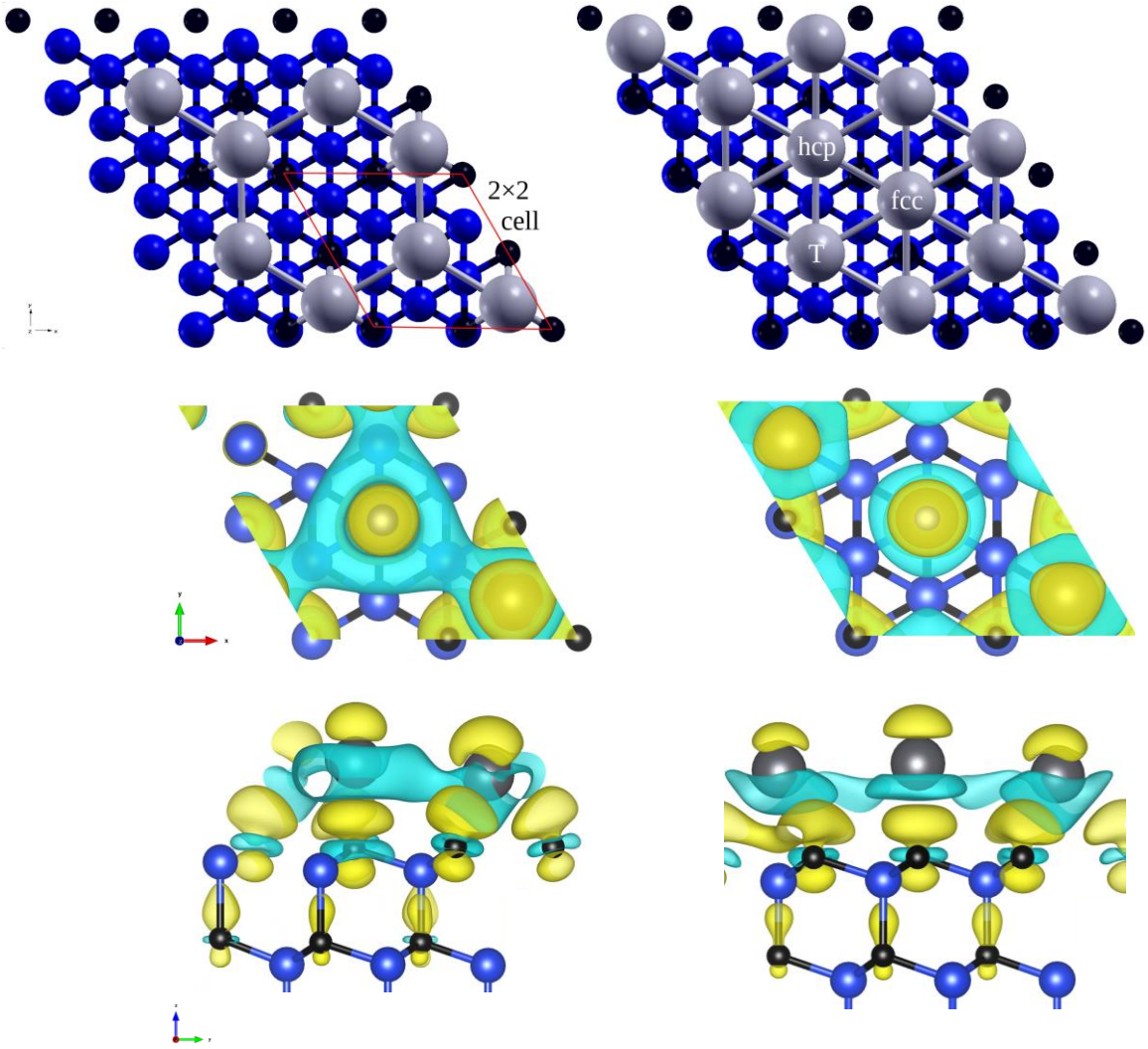

Figure 11: The honeycomb structure (1/2 ML) and he hexagonal structure (3/4 ML) on the C-face of (111) surface, with corresponding CDD graphs with izosurfaces of 2.4 me/Å^3. Side views were adjusted for better clarity.

This surface is similar to the α-SiC (0001) surface, but they differ in electronic structure. Compared to the study [111], the obtained CDD graphs show a high similarity, changes in adsorption energy with coverage show a similar trend, but the obtained energies are lower. In this case, charges accumulate in a manner analogous to previous simulations, Figure 12. Considering the bond length with Si, the obtained value (2.839 Å) is very close to the corresponding hcp position for the study of a single layer (2.835 Å) [115] and for 6H-SiC [116] (2.79 Å), but less for the fcc position (2.843 Å) compared to (2.71 Å).

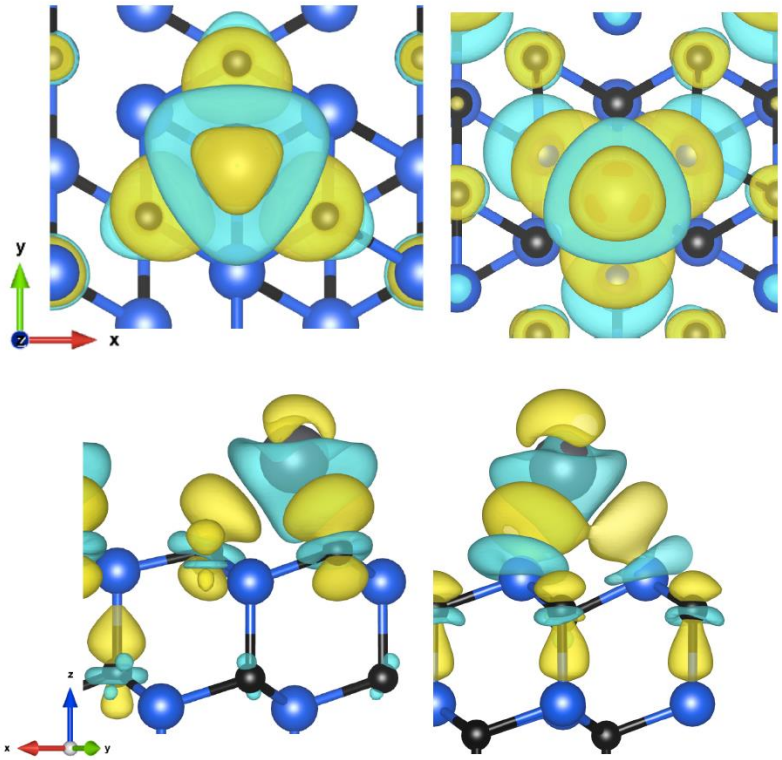

Figure 12: Top and side view of (111) surface CDD, C-face in position hcp and Si-face in fcc (isosurface values: 2.4 and 1.6 me/Å^3).

When comparing graphs for the adsorption of one, Figure 12, two, and three atoms Figure 11, it can be observed that there is a depletion of charge around the lead atom and the charge transferred to the surface. However, the amount of charge transferred to deeper layers increases. This suggests that as coverage increases, the mutual repulsion between adatoms strengthens, thereby weakening their interaction with surface atoms, and thus reducing the adsorption energy. Additionally, due to the partial saturation of orbitals, the interaction with the deeper layer strengthens, and the surface structure becomes more similar to the bulk crystal.

Acquired adsorption energies are presented in the Table 4. This surface is more even than the other two, which means that Pb-Pb interactions are not as well screened, and there is no noticeable drop in energy when transitioning to a 1/2 ML coverage. Instead, there is rather an averaging of results for corresponding positions from the lower coverage. The dense packing of adatoms on the surface forces them to shift to less stable positions.

	C – face					Si – face				
Adsorption sites	1/9 ML	1/4 ML	1/2 ML	3/4 ML	1 ML	1/9 ML	1/4 ML	1/2 ML	3/4 ML	1 ML
Top (T)	-2.65	-2.56	-3.02	-2.72	-2.39	-2.71	-2.43	-2.93	-2.77	-2.36
Charge transfer	0.78	0.69				0.25	0.15			
fcc-Hollow	-3.51	-3.39		-2.72	-2.39	-3.6	-3.53			
	0.78	0.72				0.18	0.15			
hcp-Hollow	-3.64	-3.59	-3.02	-2.72	-2.39	-3.49	-3.45	-2.93	-2.77	-2.36
	0.82	0.76				0.17	0.13			

Table 4: Adsorption energy and lead charge transfer for (111) surface

Below, band structure graphs are presented in Figure 13 and their corresponding density of states in Figure 14, normalized with respect to the Fermi energy. The (111) structures are periodic in only two dimensions, which is why the K-points path for the plane in the hexagonal lattice was used. As mentioned earlier, the GGA method does not accurately depict the characteristic energy gap between the valence and conduction bands. In this case, it is underestimated. Nevertheless, by analysing the partial density of states (PDOS), differences in states and their primary causes can be observed.

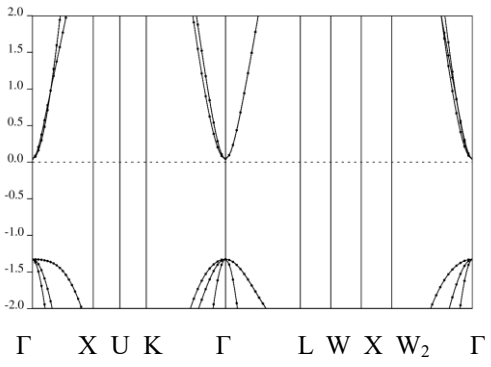

Figure 13: Band structure of 3C-SiC

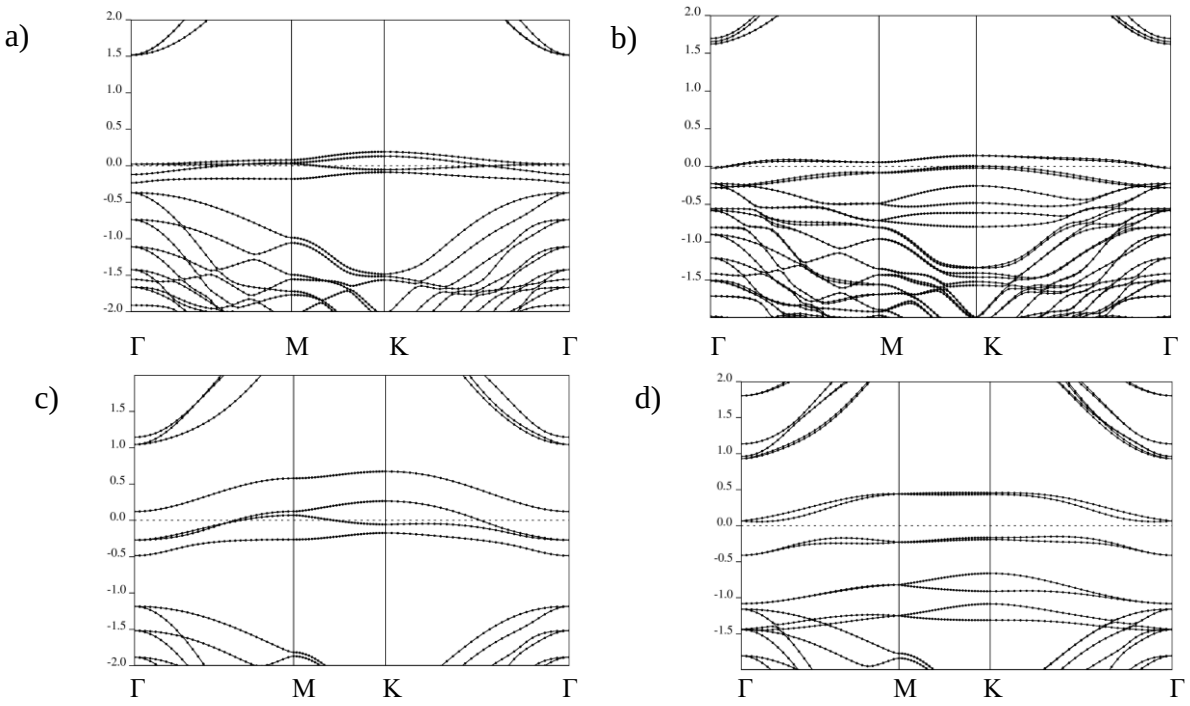

Figure 13: Band structure of a) clear (111) C-face and b) with adatom c) clear (111) Si-face d) with adatom

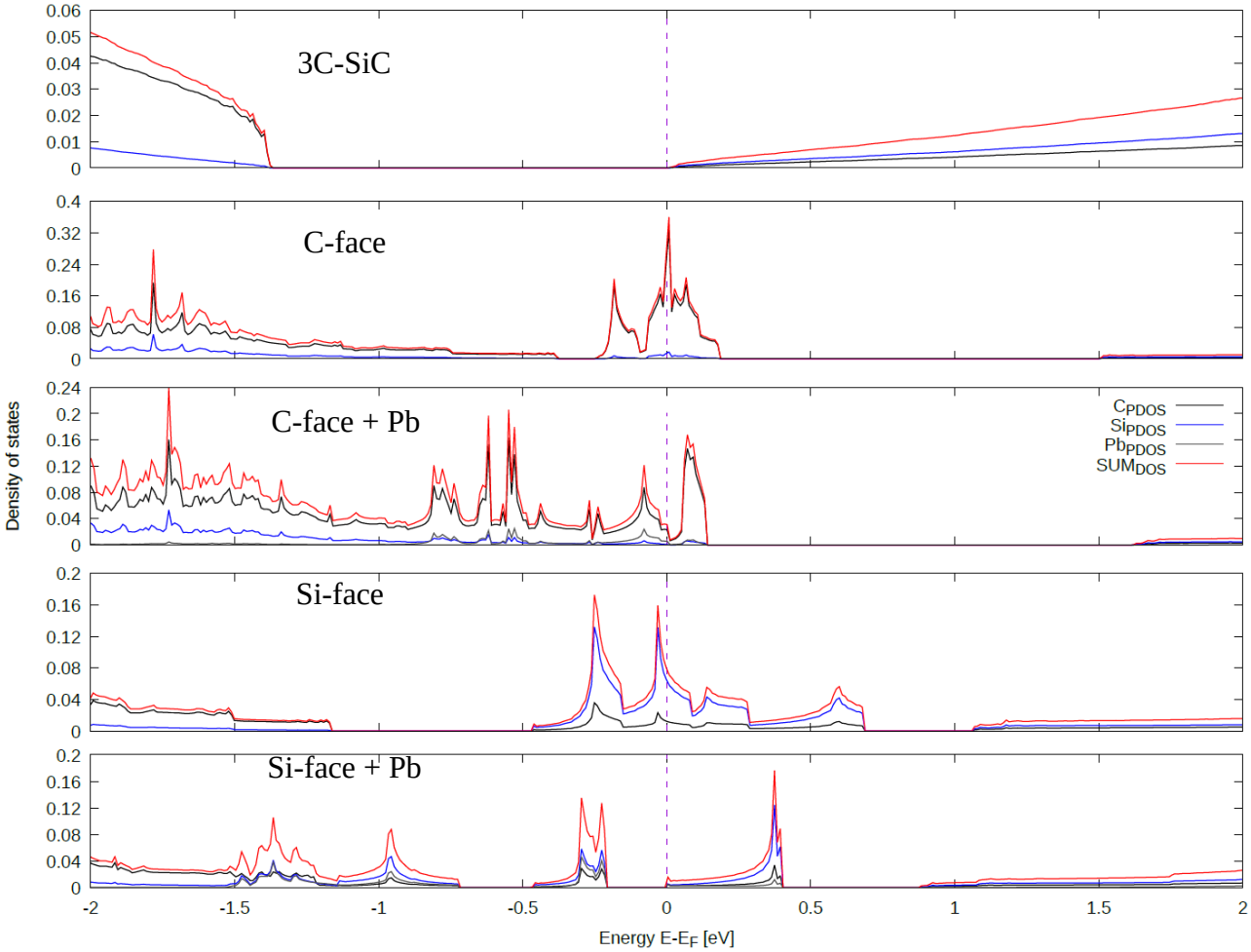

Figure 14: Partial density of states for bulk crystal, and (111) surface: C-face, C-face with adatom, Si-face, and Si-face with adatom

For the clean surfaces, the unsaturated bonds significantly influence the electronic structure. The analysis shows that near the Fermi level, the states of electrons from the hybridized p orbitals of surface atoms dominate. The energy states intersect the Fermi level, making the material cease to be a semiconductor. Once these bonds are saturated with hydrogen atoms, these properties return. On the Si-terminated surface, a significant influence of carbon's p orbitals can be observed, with both states intersecting the Fermi level. It can be observed how these states partially disappear after the absorption. Peaks originating from lead atoms, in both cases, are below the Fermi level, suggesting they are stable structures. They are lower for the C-face, proving that this structure is more stable. Silicon more easily donates electrons, and charges accumulate above the surface, unlike carbon, where states are more evenly distributed.

4.4 Analysis and discussion

From the presented study, it can be inferred that interactions with lead will lead to chemisorption. C-terminated surfaces generally show lower adsorption energies – they are more stable. Extra charges are evenly distributed around the atoms. It should be noted that for the (100) surface, these energies are overestimated due to the presence of a dimer, which reduces the number of available dangling bonds. The lower energy is due to the fact that carbon has a high electronegativity of 2.52, while silicon's is 1.82 and lead's is 1.56[126]. Hence, the charge transferred by lead is considerably higher. In the case of interaction with a silicon atom, charges accumulate above it but are also transferred to deeper layers carbon atoms, which is particularly well visible for the (110) surface. As the coverage increases, the adsorption energy generally increases, except for the transition to 1/2 ML in (100 and 110), which can be explained by the mechanism of occupying the second nearest neighbouring position, which is sufficiently distant and well screened that adatoms do not exert significant influence on each other. For the (111) surface, such screening is significantly reduced. Absorption leads to partial filling of the p orbitals on the surface, bringing its coordinates closer to those corresponding to the bulk. Increasing the coverage reduces the strength of the interaction between the adatom and the surface atoms, destabilizing the surface while simultaneously increasing the strength of the interaction with the next layer. This promotes the formation of vacancies on the surface. Carbon vacancies form more easily with activation energy of 4 eV as compared to 8 eV for silicon (in 4H-SiC) [127]. Additionally, carbon has greater mobility in crystal, making it easier to transition to the solution, resulting in the formation of an amorphous silicon layer on the surface. Releasing it from the crystal lowers the energy barrier of the reaction, which can facilitate oxidation. The obtained adsorption energies are lower than corresponding results for other polymorphic crystals [111], this may suggest a higher susceptibility to reaction with lead, but to draw significant

conclusions, broader studies are needed, considering its effect on vacancies, influence of Si rich surface and experimental validation.

4.5 Molecular dynamics simulations

Molecular dynamics simulation is a computational technique used to study the time-dependent behaviour of atomistic systems. Over time, it has proven its usefulness in physics, manly in the domains of chemistry, materials science, and the study of complex organic systems. By numerically solving Newton's equations of motion, iterated over a suitably short time step for a given system, it provides insights into the microscopic motion, allowing for the exploration of physical and chemical properties at the molecular level [128]. Integral to the success of this approach are the interatomic potentials, which guide those equations. Depending on their complexity, these potentials encompass interactions ranging from simple pair potential to those concerning bonded and non-bonded iterations. Calculations were conducted using popular open-source Large-scale Atomic/Molecular Massively Parallel Simulator (LAMMPS) software [129].

The motion of atoms over a timestep can be predicted using numerical integration methods, such as the Verlet algorithm. Forces acting on each atom F_i are calculated based on the sum of all forces, which arise from the negative gradient of the interatomic potentials V_{ij} or force fields and their respective distances r_{ij}. For a conservative force, the equation can be written as follows:

$$\vec{F_i} = -\nabla \sum_{j}^{N} V_{ij}\left(\vec{r_{iJ}}\right)$$

4.6 Methodology

In the simulations, multi-body analytical Bond Order Tersoff potentials were used to define Si-C, originally created specifically for these covalent compounds [130], and Si-O interactions [131]. This advanced model considers the environment in which the atom is located, up to second nearest neighbour, which includes the number of bonds and dependencies on their angles and lengths. The following equations dictate the behaviour of this potential:

$$V_{ij} = f_C(r_{ij})[\overbrace{A_{ij}e^{-\lambda_{ij}r_{ij}}}^{f_R(r_{ij})} \overbrace{- b_{ij}B_{ij}e^{-\lambda_{ij}r_{ij}}}^{f_A(r_{ij})}]$$

$$b_{ij} = \left(1 + \beta_i^{n_i}\zeta_{ij}^{n_i}\right)^{-1/2n_i},\ \zeta_{ij} = \sum_{k\neq i,j} f_C(r_{ik})\omega_{ij}g(\theta_{ijk}),\ g(\theta_{ijk}) = 1 + \frac{c_i^2}{d_i^2} - \frac{c_i^2}{d_i^2 + (h_i - cos\theta_{ijk})^2}$$

Where $f_R(r_{ij})$ is the repulsive and $f_A(r_{ij})$ is the attractive component, $f_C(r_{ij})$ is a function of smooth cutoff, and λ_{ij} characterizes the bond strength, b_{ij} function describes influence of neighbouring atoms k (bond order) on the interaction between atoms i and j, as it increases attraction term decreases. It is dependent on ζ_{ij}, which describes the angular effects, it is influenced by the number of bonds, it

considers the relative distances between atoms ω_{ij} and coefficients describing the intensity functions of those effects $g(\theta)$ dependant on angle θ. The potential is defined by a series of the coefficients for all combinations of atoms triplets.

Unfortunately, no sufficiently advanced potentials were found to describe interactions with lead; therefore, a classic Lennard-Jones pair potential was used [132], [133]. Due to arising conflicts with other potentials, it was also used to describe Pb-Pb interactions. Because of its simplicity, this potential is characterized by particularly good computational efficiency, making it often used for preliminary testing. Potential approximates interactions of non-bound atoms well, such as noble gases but has low accuracy on densely packed bound particles. Therefore, the results presented here should only be considered as general trends rather than precise values.

$$V(r) = 4\epsilon\left[\left(\frac{\sigma}{r}\right)^{12} - \left(\frac{\sigma}{r}\right)^{6}\right]$$

Where ϵ is depth of potential well, σ is a distance at which potential is equal to zero which can be interpreted as effective diameter of the particles, utilized potentials are shown on Figure 15, R_{min} is equilibrium distance between two particles – point of lowest energy. A significant advantage of this potential is the possibility to easily determine relationships between atoms of different types, which is not so obvious for other kinds. For this purpose, the Lorentz-Berthelot mixing rule is used [134]:

$$\sigma_{AB} = \frac{\sigma_{AA} + \sigma_{BB}}{2}$$

$$\epsilon_{AB} = \sqrt{\epsilon_{AA} + \epsilon_{BB}}$$

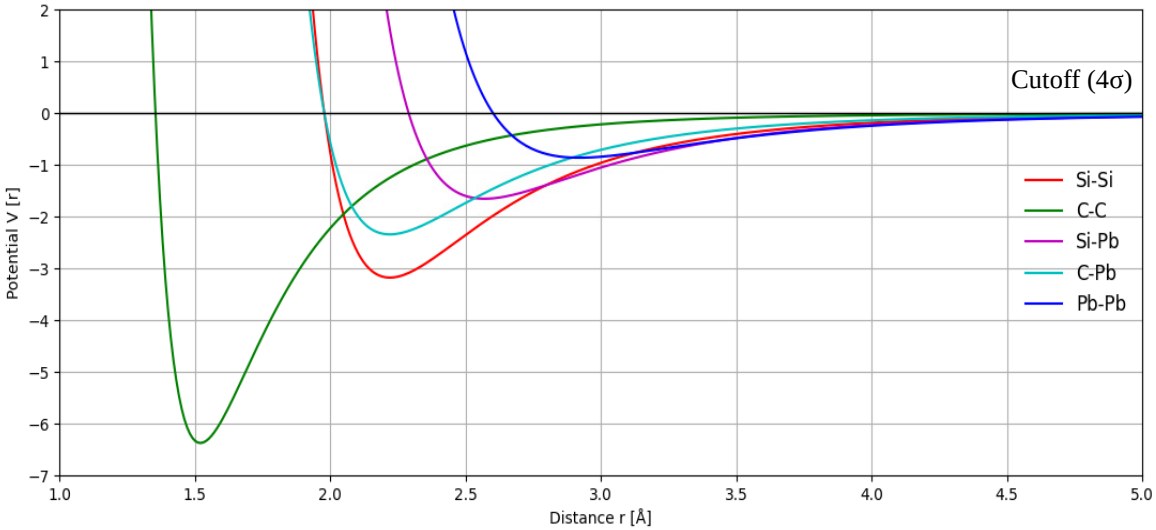

Figure 15: Utilized Lennard-Jones potentials

The simulation box utilizes periodic boundaries, meaning that atoms at the boundary interact with images of atoms on the opposite side of the box. The isothermal-isobaric NPT and NVT where volume is constant, ensembles are used for control, employing non-Hamiltonian equations in the Nosé-Hoover style for parameters control. In temperature control, particle velocity undergoes periodic adjustments, while in pressure control, the box dimensions are tweaked, N in this type names stands for constant number of particles in simulation box. The simulation procedure takes place in several crucial steps, first the energy of the entire system is minimized. Then, particles are given random velocities in accordance with the Gaussian distribution for a given temperature. Atoms are in ideal positions, so an initialization phase occurs in which atoms move to a low energy position before equilibrium is established, determined more by the specific potential used rather than preset position. For this reason, results from this phase are omitted in evaluating the obtained data. The duration of this phase is determined by analysing changes in the total energy, the target simulation begins when this energy reaches a roughly constant level. An initial lattice constant of 4.348 Å was implemented for the cubic box with side length of 15 unit cells. During the simulation under standard conditions, this constant decreased to 4.340 Å, leading to density of 3.25g/cm^3 as compared to theoretical 3.21 g/cm^3.

4.7 Results

Simulations for seven representative surfaces were conducted in the NVT ensemble for supercells with dimensions of 12×12×12 applying the earlier determined lattice constant., where a vacuum gap larger than the cutoff (4σ) was applied above the surface and the bottom layer was immobilized. As before, the first step was to simulate pure crystals to achieve the equilibrium positions of the atoms and account for changes in supercell dimensions at the surface. These simulations were conducted at a temperature of 1000°C. As a result of minimization, atoms settle in stable positions of minimum energy, allowing for a comparison to DFT calculation results, as shown in Figure16. On the (100) C-face surface, the predominant positions are LB and SB, with infrequent occurrences of the B position and almost non-existent H positions. This contrasts with DFT results, where LB and B positions were observed, and the H position had a lower energy than B. For the Si-face, dimers of Si-Si form on the pure surface, creating irregular rows. In interactions with lead, significant surface distortions are evident, with atoms preferring LB, B, and occasionally H positions. For the (110) surface, as expected, the HC position dominates, but there is a significant presence of the B position, arising from the potential for denser packing while maintaining Pb-Pb distances, with few instances of the HSi position. Atoms on the (111) C-face surface exclusively settle in the hcp position, resulting in less dense packing than the corresponding DFT calculations. On the Si-face, the predominant position is fcc, where atoms form a regular grid, while for hcp, another regular grid

forms, but at their intersection, the atoms are not in equilibrium positions, and the T position is almost non-existent. Again, this deviation suggests that the mutual repulsive force between Pb-Pb atoms is overestimated, significantly affecting the calculations. In simulations with significantly fewer lead atoms where their interactions are limited, the surface damage is much less profound, not exceeding the third atomic layer. The next Figure 17 presents another method of forming a surface by truncating the crystal with the (111) plane, where surface atoms are connected by only one bond to the atoms in the layer below. In simulations of a pure crystal, irregular dimers, trimers, and short rows of atoms formed on the surface. The positions of lead atoms are also irregular, but they dominate the spaces between the formed bonds, especially evident for the Si-terminated side, where they are even below these surface atoms layer.

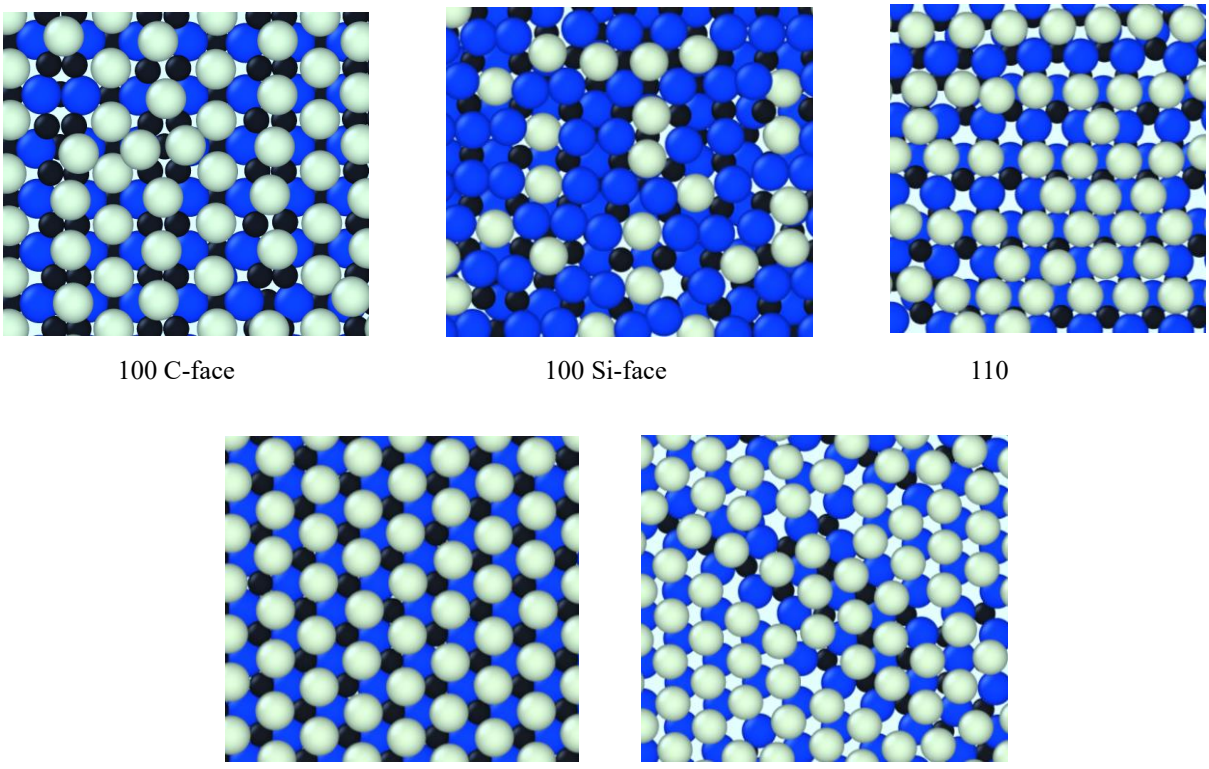

Figure 16: Surfaces after minimization, for clarity only part of the surface layer of the crystal with adatoms is shown

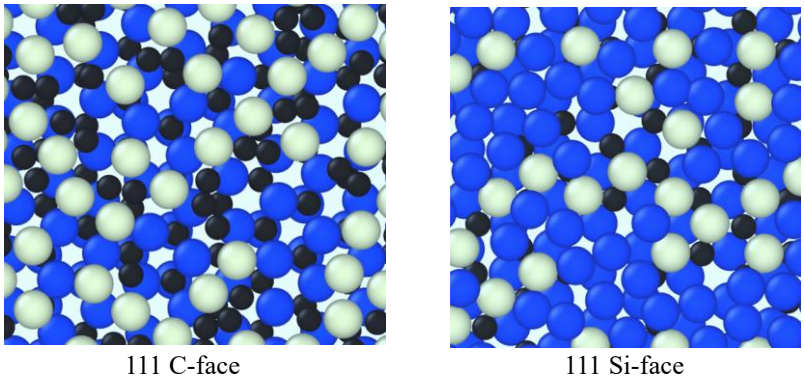

Figure 17: Second (111) plane cut – atoms on the surface have one bond to layer below as opposed to three in previous case.

Simulations conducted for all these surfaces demonstrate a dependency where, due to irregular positions on Si-terminated surfaces, metal attack is more severe in the initial phase. After a simulation time of 4 ns, these differences disappeared, and for all samples, the same surface deformation was observed, with the migration of lead atoms reaching a depth of 7 Å. The same result was obtained for the grain boundary test. The most significant changes occur in the first nanosecond, after 4 ns, a certain equilibrium is established, and the further rate of crystal damage seems to drastically slow down. To measure diffusion coefficient, Einstein's relationship for describing Brownian motion in three spatial dimensions was used.

$$MSD = \frac{1}{N}\sum_{i=1}^{N}[\vec{r_i}(t) - \vec{r}(t_0)]^2$$

$$D = \lim_{t\to\infty}\frac{MSD}{6t}$$

Where *MSD* stands for mean square displacement, three dimensional vectors are compared to reference value (at t_0), and *D* is diffusion coefficient, represented as the slope of the line fitted to the slope of the *MSD* change in time.

In the diffusion simulations, a cubic box with edge lengths of 65.22 Å was used as the initial conditions. Additional 540 lead atoms were randomly placed in interstitial positions within SiC lattice, the distances between Pb atoms are large enough that their interactions are sufficiently limited. For utilizing the ergodic hypothesis, an adequately long simulation time of 4 ns was applied to achieve proper averaging of values. As can be seen in Figure 18, the rate of change stabilizes after approximately 300 ps, so this part is excluded from the approximation of the diffusion value.

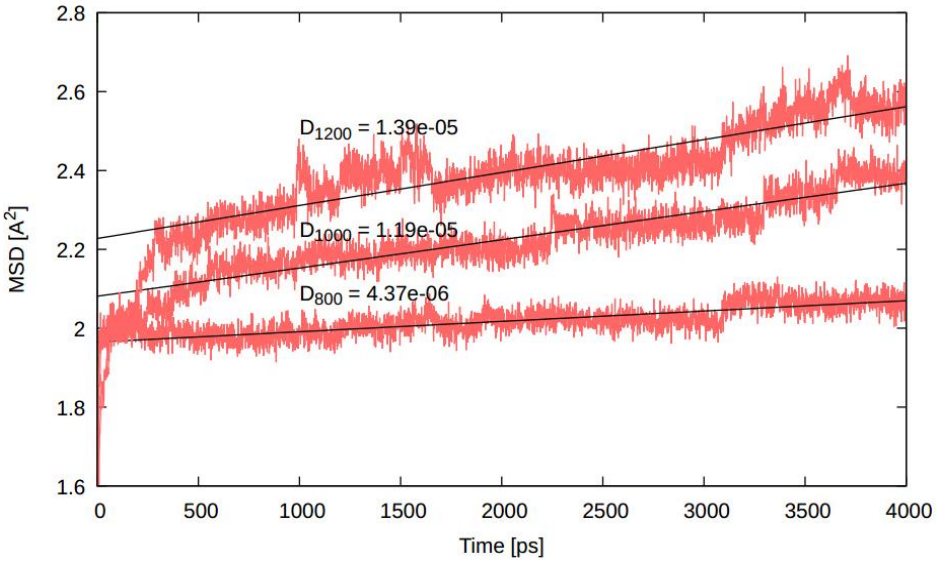

Figure 18: Fitting of diffusion coefficient to change of MSD in time, for clarity only three shown.

In the studied crystal, the presence of strong, short bonds combined with the relatively large size of the lead atom makes its diffusion energetically demanding. The displacement requires and local structural disruptions or even bond breakage, therefore, its rate increases with temperature. The resulting coefficients are as follows (m^2/s): $D_{800°C} = 4.37\times10^{-14}$, $D_{900°C} = 5.81\times10^{-14}$, $D_{1000°C} = 1.19\times10^{-13}$, $D_{1100°C} = 1.21\times10^{-13}$, $D_{1200°C} = 1.39\times10^{-13}$. Similarly, a crystal with 0.5% vacancies was evaluated, simulating the effects of significant radiation damage for every tested temperature, the diffusion value here was an order of magnitude higher. This behaviour is attributed to the appearance of vacancy diffusion, which has a lower energy barrier for this system. An amorphous structure, created by rapidly cooling a sample from a very high temperature, was investigated in test for 1000°C. This structure, with many unsaturated bonds and larger voids, demonstrated a notably higher diffusion result of 5.41×10^{-12}. For comparative purposes, tests on amorphous SiO_2 were also conducted. Acquired, results were lower, with values of 9.03×10^{-13} at 1000°C and 1.39×10^{-12} at 1200°C. This could be attributed to the compound's ionic character and thus stronger interactions with oxygen, thereby limiting metal movement. To determine the activation energy E_A and diffusion prefactor D_0, the Arrhenius equation was used:

$$D = D_0 e^{\frac{-E_A}{kT}}$$

Where k is the Boltzmann's constant, and T is temperature. To fit rate of change to the obtained data, the logarithm of the presented equation was taken:

$$lnD = lnD_0 - \frac{E_A}{kT}$$

The following values were obtained: $E_A = 4.91$ eV; $D_0 = 4.35\times10^{-12}$ cm^2/s

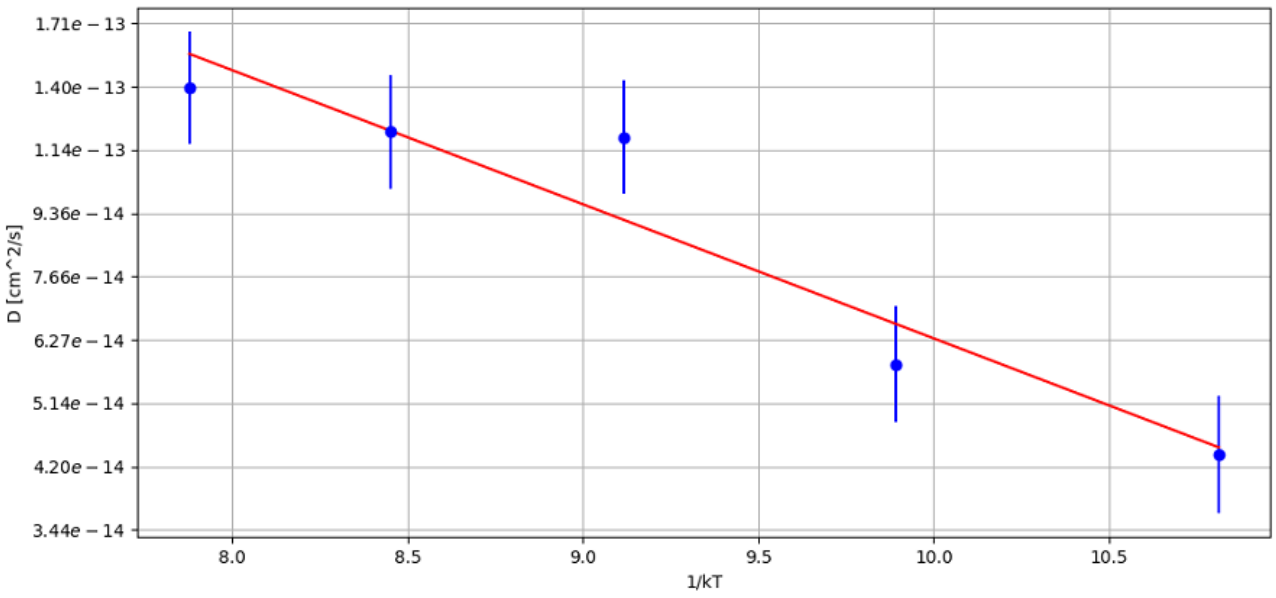

Figure 19: Diffusion coefficients as a function of reciprocal temperature scaled by factor 1/k and fitting of Arrhenius equation.

The subsequent simulations involved a crystal composed of 10×10×10 SiC unit cells inside a lead-filled cubic simulation box with edge lengths of 98 Å. To immobilize the sample but to ensure that it will not have a significant impact, the positions of four atoms in the centre of the cube were fixed in their bulk positions. The following Figure 20 illustrates the degradation rate of the cube, by analyse of the changes in the number of diamond crystal structures over time. Again, initialization phase should be disregarded in this analysis. The subsequent relationship appears parabolic, suggesting of diffusion-driven corrosion. An additional Figure 21 provides a cross-section of this supercell.

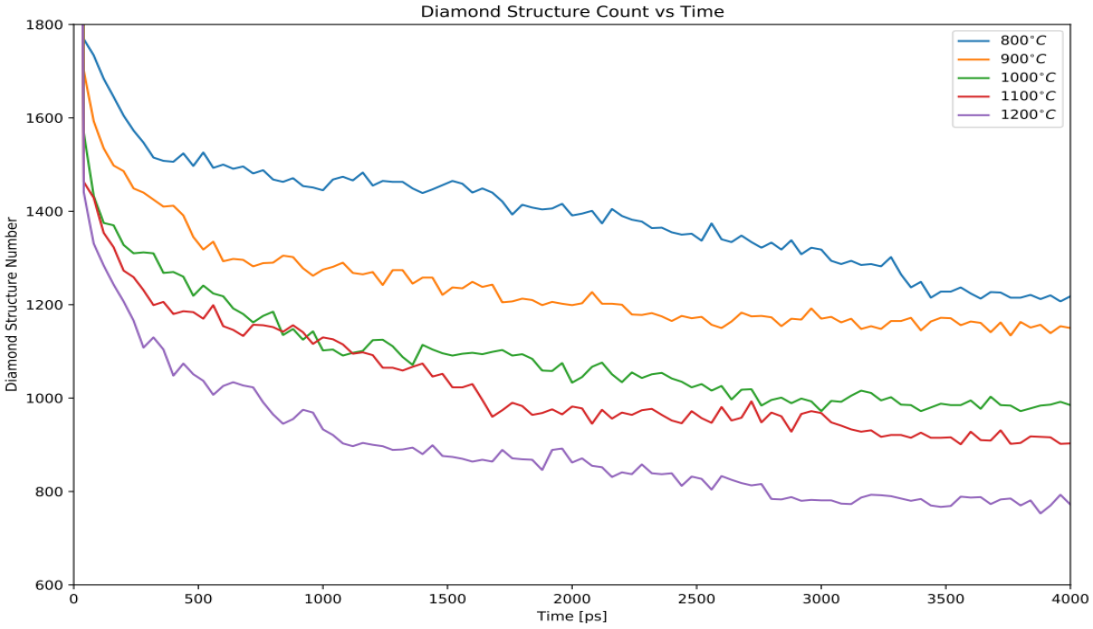

Figure 20: Rate of change in diamond structure number in time for different temperatures

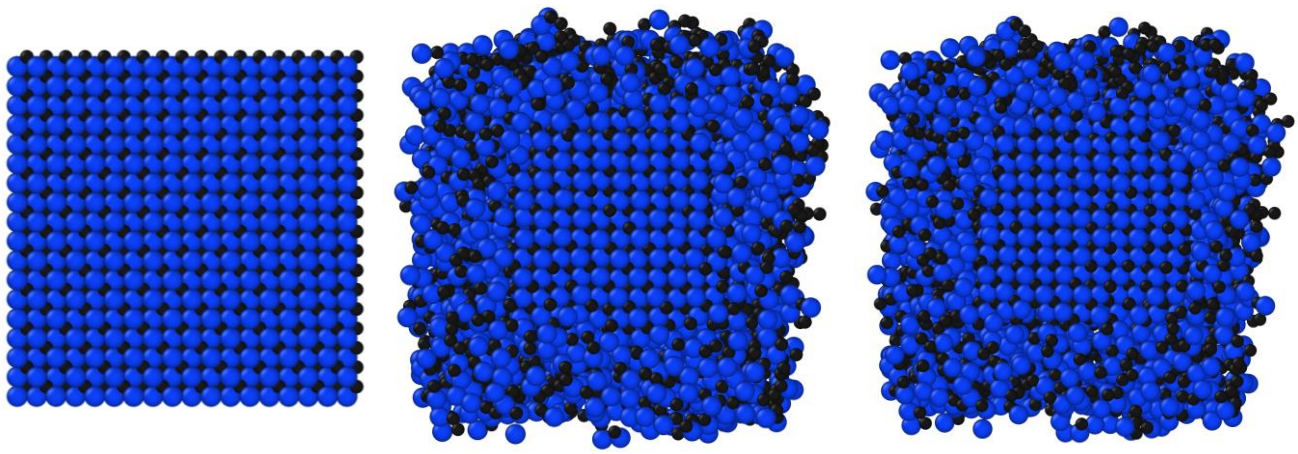

Figure 21: Cross section of SiC crystal embedded in Pb, before simulation, after 5 ns and after 10 ns in 1000°C

From the analysis, it becomes clear that the rate of degradation significantly slows down following the initial phase, and subsequent changes are rather subtle. Only a few Si and C atoms fully detach from the structure, and they do so in comparable amounts. An amorphous layer that forms on the surface exhibits stratification, dominated by carbon atoms on the outermost layer. These smaller carbon atoms, when released from the crystal lattice, migrate more easily. This newly formed layer contains lead atoms but still retains most of the original bonds, and also forms new ones with adatoms. As a result, further diffusion into the structure becomes progressively restricted.

4.8 Analysis and discussion

The preliminary study presented here examines the impact of lead on various representative surfaces, the diffusion of metal in the crystal at different temperatures, and in the amorphous form of silicon carbide and silicon oxide. It also investigates the rate of surface degradation for a crystal immersed in a liquid. For this study, apart from Tersoff potential, a classic Lennard-Jones pair potential was used. This type of potential performs well for gases but loses accuracy in denser substances, especially since different types of atoms were used. As a result, the findings do not align with DFT calculations. The density distribution of adatoms monolayer is significantly lower than in the previous study, suggesting an excessive repulsive force between these atoms, which significantly affects surface degradation tests. No differences in material degradation were observed depending on the exposed surface and for the grain boundary test. Nevertheless, the simulations confirm certain dependencies: the diffusion rate significantly increases with temperature, material degradation progresses at a parabolic rate, carbon released from the crystalline structure easily migrates to the surface, and assuming that atoms completely separated from the surface are classified as dissolved, the solubility of Si and C is similar. The obtained activation energy (E_A = 4.91 eV) as expected are higher and diffusion values are lower than those for significant in this matter fission products like Ag with 2.23 eV or Pd and Ru [135].

Recently, innovative methods have emerged that incorporate the smooth overlap of atomic positions technique, combined with the Gaussian approximation potential in machine learning, to devise new potentials [136]-[138]. This approach will pave the way for achieving precise potentials in future research.

V Microdemonstrator loop

Designing a safe and reliable reactor, especially of a new type, is a complex process that often necessitates conducting extensive new research and experiments. One such experiment for the Dual Fluid Reactor is the currently under-construction micro-demonstrator (μD), a double-loop experiment. This project is being conducted on behalf of Dual Fluid Energy Inc., in collaboration with specialists from the HITTEC Nuclear Equipment Division, located at the National Centre for Nuclear Research. It serves as a prototype laying the groundwork for a subsequent, more advanced experiment—namely, the mini-demonstrator (mD)—which will be more closely aligned with the final reactor design [139]. The main objectives of the experiment include: the practical validation of computational fluid dynamics models and thermohydraulic calculations; corrosion tests with a flowing medium at varying temperatures; the analysis of the heat exchanger's geometry; the empirical study of natural convection[10], [11], [140], [141]; and additionally, gaining experience in the design and operation of this type of facility. The design is largely inspired by the TALL-3D research unit owned by KTH [142]-[144].

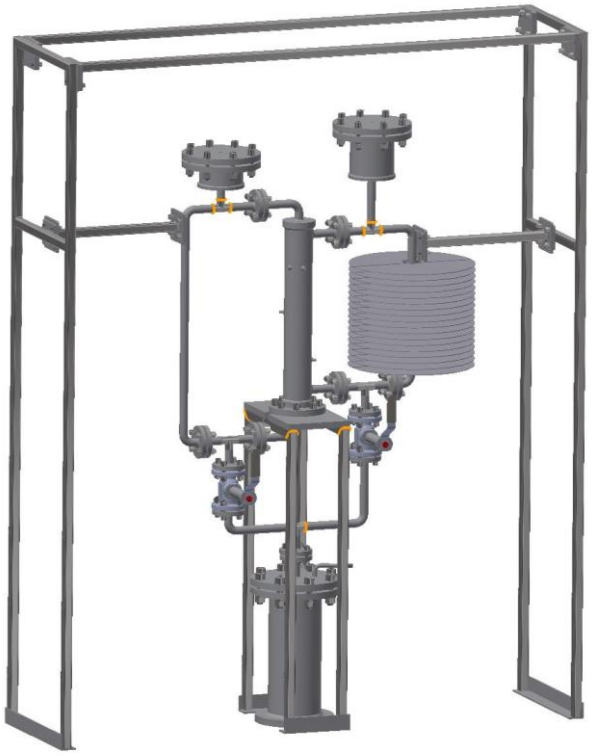

Figure 22: Project of microdemonstrator loop facility

5.1 Experiment facility details

The unit consists of two independent loops: the "hot" loop corresponding to the fuel loop, and the coolant loop. Liquid lead will flow through both, while the void spaces will be filled with an inert gas – argon to limit the negative impact of oxygen. Both loops intersect at the central element of the heat exchanger, where a single "hot" channel runs through the centre and is cooled by the surrounding metal. This relatively simple design is merely an initial variant and can easily be replaced with a more advanced part at a later time. Such an approach also applies to other components, representing a deliberate step-by-step development strategy aimed at identifying and resolving potential issues while their consequences are not yet severe, before constructing a more complex system. The construction is modular; the modules are connected with flanges. This implies that, if necessary, a specific module can be easily replaced. Furthermore, the structure can be conveniently expanded with additional components. All pipes, including the cooler, valves, sensors, and connections, are surrounded by heating cables with the estimated maximum required heating power being about 3 kW and thermal insulation, except for the cooler. For the "hot" leg's heating section, an independent heating part has been incorporated. The entire setup is mounted on a frame, allowing for wall attachments, thus forming a separate room. For safety reasons, this room will be closed during operations. An independent air filtration system will also be installed due to the toxicity of lead vapours. All control-related components are externalized. The project's maximum temperature is set at 500°C, but the target operating temperature will be 450°C with a temperature difference of 50°C between the inlet and the outlet of the heat exchanger. All parts that come into contact with lead will be made of stainless steel 316L, which is characterized by its reduced carbon content. As experiments show, after an oxy-nitriding treatment, this steel at these temperatures will exhibit increased resistance to lead exposure [145].

5.2 Main tank

The tank located at the lowest point of the unit serves multiple significant roles. The first of these is preparation—cleansing and controlling all the lead that will subsequently be melted. The tank has its own independent heating system. Its volume is larger than what the current configuration would require; a height buffer is maintained to provide space for gas compression as well as for future planned components. Another function is system filling, which takes place by pressurizing the tank with argon gas. Here, the gas acts similarly to a piston, pushing out the liquid to fill both loops.

During the draining process, a cushion of gas prevents the lead from striking too forcefully, as this could damage the tank and even the entire structure. The slowly released gas can be recompressed back into cylinders. Despite the tank's thick walls, its mass will be less than that of the lead; for this reason, a reinforced bottom has been used, which for added stability has an increased diameter. The thermocouple's protective conduit visible in the drawing is designed in such a way that allows for its replacement. Thanks to the small diameter of the thermocouple, down to even 0.5 mm, it is flexible, allowing for such an installation.

Figure 23: Main tank cross-section with visible gas inlet, lead outlet and thermocouple channel

5.3 Heat exchanger

The most crucial component of the unit is the centrally located heat exchanger, where the most essential processes for the experiment will take place. As previously mentioned, the heat exchanger consists of a central pipe in which hot lead flows, and a considerably wider external pipe through which the cooling lead flows. As depicted in the Figure 27, the core contains thermocouple protective tubes set radially, allowing for radial measurements at three different heights Figure 24. The height of this part is half a meter. Due to the potential for vibrations, the heat exchanger is further reinforced and has its own frame. A counter current flow in line with the force of natural convection is anticipated, but with the use of a pump, cross-current flow can also be examined. In later versions and also in the mD, a more complex system with either seven or a 37-tube bundle will be studied. The design also allows for the examination of modern solutions like the high-efficiency Printed Circuit Heat Exchanger [146], [147], considered for use in high-temperature fourth generation reactors, and the recently described 3D printed gyroid-shaped heat exchanger [148]. These studies are intriguing on their own but also hold significant potential to prove beneficial in reactor technology.

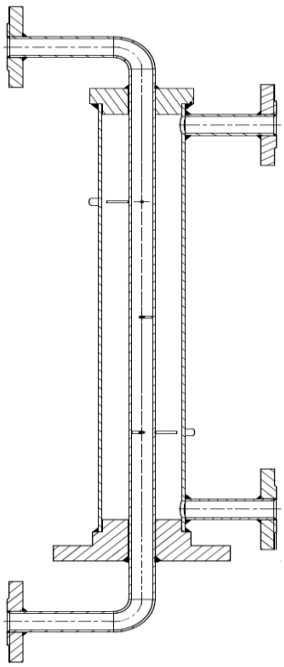

Figure 24: Heat-exchanger cross-section, with thermocouple channels visible

5.4 Expansion tanks

These tanks are located at the highest point of both loops, at the same elevation. One of their primary functions is to collect the excess volume of lead generated by the effects of thermal expansion. They are mostly filled with gas, serving as a pressure stabilizer. Their volume is half of the liquid volume in the respective loop, considering additional planned components. In the tee joint of the cooling loop tank, a throttle will be installed to limit the flow of coolant. This is for better control of cooling performance, reducing the risk of over-cooling the liquid and its potential solidification in the pipe. In this case, only partial flow restriction is needed, so a simplified solution was chosen instead of an additional valve. These tanks also contain liquid level sensors that provide information on the filling status of the loops and the degree of filling of these tanks. External pressure sensors are attached as well, serving as an initial alarm system indicating any leaks.

5.5 Radiator

In this section, heat is directly dissipated into the air, which is why this component lacks insulation. Eighteen fins have been applied, each with a specialized attachment system that allows for adjustment in both number and spacing. If necessary, a fan will be employed to enhance cooling efficiency. The height of the radiator will be shorter than that of the heat exchanger due to the need to attach the mounting bracket. Preliminary heat exchange analysis has shown that this size is fully adequate for cooling the liquid.

Figure 25: Heat radiator with adjustable fins

5.6 Pumping system

The current configuration does not yet include a pump, but after conducting a series of tests concerning natural convection, it will be installed in the coolest part of the cooling loop - behind the radiator. The heating loop, similar to the reactor project, will not contain a pump, and the flow will be forced solely by the force of natural convection. Due to the considerable risk of erosion, magnetohydrodynamic pumps are the most suitable, regardless of their type, they have low efficiency but contain no moving elements within the liquid stream. Two options operating on different principles are considered.

The first one is a simple pump, like the one in the TALL 3D Figure. It works on the principle of inducing eddy currents in the fluid by rotating discs with permanent magnets on both sides of a flattened, arc-shaped pipe, which forces the fluid flow. This is a decidedly simpler and cheaper solution, but it has some disadvantages. This part of the pipe must be uninsulated, which can be problematic in case of motor failure. The magnets must be close to the pipe, risking exceeding their Curie temperature. Motor vibrations may affect the circulation and risk damaging the discs; hence it should be mechanically isolated from the system. Additionally, this method will generate extra heat, which must be considered in calculations.

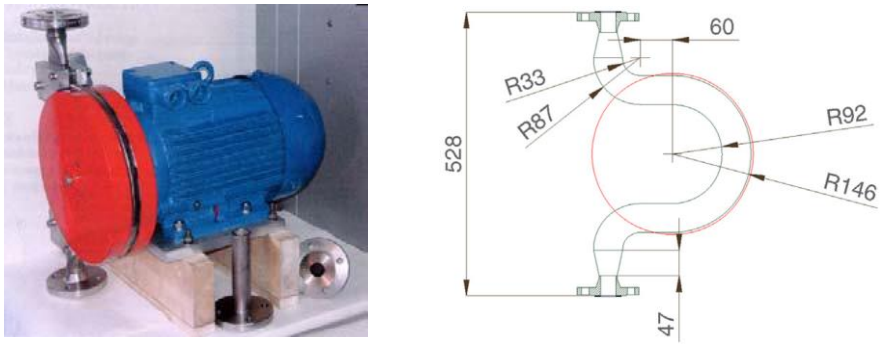

Figure 26: Magnetic pump by [144] and [142]

The second pump considered operates on the principle of the Lorentz force, which arises as a result of the movement of charged particles forced by a voltage difference in a magnetic field [13], [149]. This type of pump is likely to be ultimately used in the reactor. It consists of two parallel plates of an electrical conductor and two perpendicular insulating plates with electromagnets outside. This pump is expensive, with its cost comparable to the price of the entire circuit. This is due to the need to use resistant materials, especially since the electrodes are in direct contact with the liquid. Additionally, there are special power requirements - low voltage and high current, necessitating the use of additional equipment.

5.7 Sensors

The use of thermocouples for temperature detection has been chosen due to their wide operating temperature range and high accuracy. The layout of the thermocouples is presented in the Figure 27. A decision was made to create permanent enclosures for the thermocouples because other methods of securing them, such as additional sealed holes, pose additional leak risks. Moreover, flanges would create thermal bridges due to their relatively large additional volume. While this solution is not a complete guarantee of safety, dedicated closures will be additionally mounted at the end of the hole for added security.

In the heat exchanger, the layout of thermocouples is radial. Both the thermocouples measuring the temperature in the heating pipe and in the cooling, pipes are arranged at 120-degree angles relative to each other at three different heights and 60 degrees from each other on one level. This is to minimize the effects of the thermal bridge that may be created. The diameter of the enclosures is intentionally larger to allow the insertion of two or more thermocouples and to manipulate their depth.

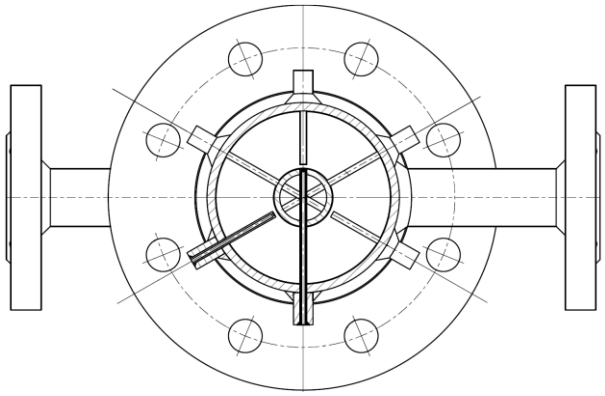

Figure 27: Top view of heat-exchanger with visible thermocouple channels in radial arrangement

External thermocouples are also planned, located outside the pipes at key points in the loop, such as before and after the heater and radiator. These correspond to the inlet or outlet to the heat exchanger, taking losses into account. The thermocouple in the main tank is positioned in such a way as to avoid conflict with the flange and to be attached to a rigid pipe to minimize forces acting on it during rapid liquid descent. The thermocouple enclosures will bend above the liquid level, so the effects of any interactions should be minimal. The thermocouples and their stiffened, smaller diameter wires are flexible enough to easily adapt to this bend in the enclosure. The length of the enclosure is also designed for the possibility of adjusting the height of the thermocouple depending on, for example, the total height of the lead. To avoid interference, the thermocouple wires should be relatively short; therefore, the data collection unit should be as close as possible. To avoid voltage spikes, these units will be placed on electrically insulated shelves. Data cables with amplified signals

will be routed outside the room to the main control unit, but an on-site feedback-based power control system can also be employed.

The working temperature of the loop significantly narrows down the choice of flowmeters[150], [151], which is why a Lorentz force flowmeter is planned for measuring flow velocity[152], [153] This simple-to-construct sensor provides information about the average flow velocity of the fluid but not about the velocity profile. In a device built similarly to the basic pump design with two disks, the angular velocity is linearly dependent on flow velocity. For operation, at least a section of non-insulated pipe and a minimal distance from it are necessary. Extending the length of the fluid's interaction path is beneficial, making elbows in cooler parts of the loops (those located lower) the most appropriate locations. The sensor should be relatively small to minimize its impact on flow; a photocell could be mounted next to it for speed measurement, allowing for external insulation to reduce heat losses. The sensor works similarly to the pump; in this case, force is exerted on the disk by the circulating eddy currents. A more advanced sensor that provides information on the velocity profile is, for example, a Doppler effect flowmeter [154], [155]. It works on the principle of emitting, reflecting, and measuring ultrasonic waves from contaminants in the fluid, such as micro-bubbles of inert gas that may be introduced into the loop. This solution requires direct contact with the liquid and is therefore more sensitive to high temperatures; however, this can be mitigated by using a sufficiently long acoustic wave guide [154]. The use of a dedicated connection with a diaphragm seal is also necessary to allow free vibration of the rod.

If sufficiently long valve handles are considered, actuators or electric motors are not necessary for their control. However, their use is advantageous for possible automation of lead drainage, significantly reducing reaction time in case of leak detection. Automating this process would not only improve efficiency but also enhance the safety measures in place, allowing for quicker response in emergency scenarios.

In the current project, only gas pressure gauges are incorporated. For future improvements various sensors are considered for implementation: those providing absolute pressure readings with diaphragm seal as well as a more sophisticated arrangement specifically designed for measuring relative pressure with liquid medium.

For the latter, the incorporation of an additional heating system is essential. This system operates continuously during the circuit's activity to counteract temperature differences. The setup also employs a supplementary working medium, such as oil, whose pressure is mechanically compared in a distinct unit. When interfacing with metal components, diaphragm seals are utilized.

At higher flow rates, mechanical vibrations will occur. This phenomenon will also be the subject of future research due to its potentially adverse consequences. To counter material fatigue, a passive mechanical damping system will be incorporated in other tests. For periodic checks on insulation and functionality, as well as for the detection of potential thermal bridges, thermal imaging cameras will be utilized. For precise gas leakage site detection, water mixed with detergent will be used, which will foam at the location of gas escape.

5.8 Oxygen measurements and composition control

Oxygen concentration in a solution can be controlled in multiple ways. In this system, two methods will be employed. The first involves passing cover argon gas through a reactive metal purifier at elevated temperatures, where oxygen is absorbed. The second relies on the addition of a precisely measured amount of lead oxide. Additionally, a small concentration of reducing hydrogen may be included in the shielding gas maintained over liquids and circulated during maintenance operations. Though introducing hydrogen directly into the liquid would be more effective, this approach can lead to undesirable side reactions, which are particularly prominent at high temperatures.

For liquids, active oxygen control should be implemented by using oxygen sensors and pumps [156], [157] This approach is likely to reduce maintenance demands. Pumps that utilize yttria-stabilized zirconia as the solid electrolyte are prime selection for this application due to their mechanical durability and elevated ionic conductivity at high temperatures. The electrodes used are thin, making them susceptible to degradation. To mitigate this issue, a bypass channel with substantially reduced flow rates will be incorporated. High-precision, high-temperature online oxygen sensors [158], [159] share structural similarities with those pumps, on the opposite side of the solid electrolyte, reference electrode is placed, for instance from Cu/Cu_2O. At lower temperatures, the efficiency of these pumps and sensors significantly drops thus rendering them inefficient for use in μD system.

If deemed necessary, a gettering method involving graphite may be applied. Although carbon can dissolve into the solution, its solubility at the operating temperatures of the circuit will be negligible and should not result in detectable differences. However, in mD system, even over relatively short experimental durations, carbon may have an impact on the material's corrosive dissolution, which should be considered when interpreting results. This also presents an intriguing avenue for future research as it may reduce corrosion. The risk of clogging due to deposition will be minimized through channel cleaning during maintenance operations.

5.9 Corrosion Experiment Description

This research unit is specifically designed to conduct long-term corrosion experiments. Although the temperature range does not meet the ideal conditions for the intended study, the model's capacity to operate over extended periods will yield valuable insights. Samples will be securely mounted on multiple points along the internal walls of the pipes, facilitating a simultaneous assessment of the influence of temperature and flow rate. Furthermore, this experimental setup offers a unique opportunity to incorporate irradiated samples, thereby expanding the scope to investigate radiation-induced changes. A future model, designed to operate at much higher temperatures, will feature entire pipes made from silicon carbide. This will offer more precise testing conditions that better represent the geometry of a reactor, enabling the study on areas like particularly vulnerable inlet and outlet zones.

Additionally, this experimental arrangement also allows for the corrosion analysis of the steel construction material itself. Research shows that also here, factors such as oxygen concentration in the solution [160]-[162] and flow rate [23], [163], [164], affect corrosion. A balanced level of oxygen can create a stable protective layer, while too high oxygen levels leads to formation of scales that can be swept away by flow [165], and with too low level, this layer is not produced, and dissolution corrosion dominates [166]. Given these challenges, an oxy-nitriding process has been employed to enhance the steel's resistance to corrosion.

Previously described interactions with steel, oxygen, as well as carbon (in solution) were measured at higher temperatures than predicted for the loop, however, it is highly likely that they also will occur here but at a significantly lower rate. Therefore, in experiments dedicated to corrosion the selection of parameters specific to the samples can be afforded. However, in the mD, it is crucial to carefully select materials to avoid interference.

5.10 Preparation and control of experiment

Before the initial startup and later during maintenance, lead is melted in a tank and kept at elevated temperatures for several hours to allow impurities to float to the surface. These impurities are then collected from the tank. Preparing the unit for operation is done in several steps [144]. To purge the loop of gases, it is first evacuated by a vacuum pump and then filled with an inert gas – argon. This step is repeated three times. To perform a leak check, the gas is maintained under increased pressure for an extended period to examine if there are any changes in pressure. The entire unit, including valves, supply pipes, and measuring instruments, is gradually heated above the lead's melting point. The pump channel is heated by operating the pump and inducing heat in the pipe material. This is essential to prevent lead solidification and clogging in the pipes, and to avoid potential damage due to thermal stresses. Afterward, the liquid is gradually forced into the circuit by

increasing the pressure of the gas supplied to the melting tank while simultaneously releasing the gas from the valves in the expansion tanks until the liquid reaches their level. The pump is turned off during the filling and is restarted immediately afterward. In this case, the static pressure of the lead will be around 1.5 bar, and such additional gas pressure will be needed to fully fill the loop. The last step involves quickly closing all valves, which separates the two circulation systems, but the heating is maintained. Once the desired temperature is reached, it is turned off. In the current configuration, no additional heating is needed during operation of the loop, heat generated in the hot leg is sufficient. The loop control will be performed using a power control unit based on feedback from temperature readings behind the heating element. The flow rate will also be adjusted in this manner by adjustment of the throttle valve, modulating the rotational speed of disks or adjusting the power parameters in the DC pump based on speed measurements. Shutdown and emptying involve sequentially turning off the heating and cooling the liquid while simultaneously heating the tank above the melting temperature. Then, the valves are opened, and the liquid is returned to the tank through the slow release of gas. During all operations involving potential contact with liquid metal, appropriate high-temperature-resistant protective clothing, gas masks with filters and face shields will be used to protect against accidental splashes of hot metal. A container with fine gravel will be held in the room, which, if necessary, will be used to absorb the metal.

5.11 Analysis and discussion

The research facility presented here serves as a milestone on the path to constructing a DFR reactor. It is the preliminary step in creating more advanced units that more accurately reflect the reactor's design. In addition to its research functions, this facility will also serve educational and demonstration purposes to promote this technology. With this in mind, the system is laid out in a way that makes it easy to locate and identify individual components despite their being covered by insulation. Its unique construction allows for easy maintenance, project manipulation and future expansion. Despite its small size and lower operating temperatures, conducting long-term studies will provide valuable data on both SiC and steel structural material corrosion.

The planned expansion of the loop will enable studies beyond just heat exchange, corrosion, and natural convection. These will include research dependent on fluid flow rates, counter-current flow effects, velocity distribution measurements, pressure differentials, and induced vibrations. Moreover, if a direct current magnetohydrodynamic pump is employed, a series of additional tests can be conducted to optimize its operational parameters.

VI Summary

This document presents, a novel DFR technology, highlighting key chemical interactions between the metallic fuel, coolant, and the structural material silicon carbide. This refractory ceramic is characterized by high chemical resistance, and with its composite form provides outstanding mechanical durability. The most appropriate type of fibre is HiNicalon S, and combined with production methods like a combination of CVI and CVD it ensures the highest quality of the target material. The high operating temperature of the reactor creates extreme working conditions, intensifying both physical and chemical interactions. Based on the analysis of available research, dominant mechanisms during long-term corrosion for both circuits have been identified. For the coolant, these mechanisms are dissolution and oxidation. The chemical specificity of lead allows for the formation of a passivated silicon oxide layer, effectively protecting the material and providing a surface repair mechanism. Silica significantly reduces the diffusion of oxygen, reaction by-products, and even fission products. However, due to a shift in chemical equilibrium, there is a risk of active – destructive oxidation, necessitating special control measures. High-temperature studies for a clean surface indicate that the maximum safe coolant temperature should not exceed 1100°C. In the fuel circuit, dissolution corrosion will dominate. Due to the high stability of uranium oxide, it is necessary to maintain a low oxygen concentration, preventing the formation of silicon oxide. As a result of reactions with chromium, a protective layer of its silicides will form on the surface, but it is not as effective as silica, hence carbon will be continuously released into the solution.

Despite its highly desirable properties, the cubic form of silicon carbide is not as well understood as other polymorphic forms. Therefore, to determine the microscopic corrosion mechanisms, molecular dynamics simulations of interactions with lead have been conducted. The results indicate a high activation energy for diffusion, suggesting that lead will not significantly penetrate the material. Adsorption simulations using DFT show that this crystalline form is more susceptible to corrosion in lead than hexagonal forms. Comparing the interactions of three representative surfaces, the stability of the system was demonstrated in the order of (111)> (110)> (100). As expected, the most resistant was the Si-terminated (100) surface, showing the lowest coverage also in the MD model.

Based on the gathered information, possible ways to limit corrosion have been identified: for the coolant, this involves pre-oxidation of the material and maintaining the oxygen level within an appropriately high concentration range. For the fuel, this includes the application of protective coatings such as Y_2O_3 or Mo, as well as doping materials to reduce the charge of carbon vacancies. The work also includes a detailed description of the experimental unit currently under development, intended for corrosion testing and validation of simulation results.

References

[1] A. Huke *i in.*, „Dual-fluid reactor", w *Molten Salt Reactors and Thorium Energy*, Elsevier, 2017, s. 619–633. doi: 10.1016/B978-0-08-101126-3.00025-7.

[2] A. Huke, G. Ruprecht, D. Weißbach, S. Gottlieb, A. Hussein, i K. Czerski, „The Dual Fluid Reactor – A novel concept for a fast nuclear reactor of high efficiency", *Annals of Nuclear Energy*, t. 80, s. 225–235, 2015, doi: 10.1016/j.anucene.2015.02.016.

[3] D. Weißbach, G. Ruprecht, A. Huke, K. Czerski, S. Gottlieb, i A. Hussein, „Energy intensities, EROIs (energy returned on invested), and energy payback times of electricity generating power plants", *Energy*, t. 52, s. 210–221, 2013, doi: 10.1016/j.energy.2013.01.029.

[4] J. Sierchuła, „Determination of the liquid eutectic metal fuel Dual Fluid Reactor design".

[5] J. Sierchuła, D. Weissbach, A. Huke, G. Ruprecht, K. Czerski, i M. P. Dąbrowski, „Determination of the liquid eutectic metal fuel dual fluid reactor (DFRm) design – steady state calculations", *Int J Energy Res*, t. 43, nr 8, s. 3692–3701, 2019, doi: 10.1002/er.4523.

[6] D. Weiβbach, J. Sierchuła, M. P. Dąbrowski, K. Czerski, i G. Ruprecht, „Dual Fluid Reactor as a long-term burner of actinides in spent nuclear fuel", *International Journal of Energy Research*, t. 45, nr 8, s. 11589–11597, 2021, doi: 10.1002/er.5302.

[7] I. A. E. Agency, „Status of Fast Reactor Research and Technology Development", International Atomic Energy Agency, 2013 https://www.iaea.org/publications/8667/status-of-fast-reactor-research-and-technology-development

[8] X. Wang, „Analysis and Evaluation of the Dual Fluid Reactor Concept", 2017.

[9] C. Liu, X. Li, R. Luo, i R. Macian-Juan, „Thermal Hydraulics Analysis of the Distribution Zone in Small Modular Dual Fluid Reactor", *Metals*, 10/8, s. 1065, 2020, doi: 10.3390/met10081065.

[10] Y. Chikazawa, M. Konomura, T. Mizuno, M. Mito, i M. Tanji, „A Conceptual Design Study of a Small Natural Convection Lead-Bismuth–Cooled Reactor Without Refueling for 30 Years", *Nuclear Technology*, t. 154, nr 2, s. 142–154, 2006, doi: 10.13182/NT06-A3724.

[11] J. J. Sienicki i P. V. Petkov, „Passive Safety of the STAR-LM HLMC Natural Convection Reactor", w *10th International Conference on Nuclear Engineering, Volume 2*, Arlington, Virginia, USA: ASMEDC, 2002, s. 659–666. doi: 10.1115/ICONE10-22290.

[12] I. A. E. Agency, „Liquid Metal Cooled Reactors: Experience in Design and Operation", International Atomic Energy Agency, Text, 2008 https://www.iaea.org/publications/7945/liquid-metal-cooled-reactors-experience-in-design-and-operation

[13] M. Nowak, M. Spirzewski, i K. Czerski, „Optimization of the DC magnetohydrodynamic pump for the Dual Fluid Reactor", *Annals of Nuclear Energy*, 174, 109142, 2022, doi: 10.1016/j.anucene.2022.109142.

[14] D. Böhm *i in.*, „New Methods for Nuclear Waste Treatment of the Dual Fluid Reactor Concept", *Acta Phys. Pol. B*, t. 51, nr 3, s. 893, 2020, doi: 10.5506/APhysPolB.51.893.

[15] J. J. Laidler, J. E. Battles, W. E. Miller, J. P. Ackerman, i E. L. Carls, „Development of pyroprocessing technology", *Progress in Nuclear Energy*, 31/1, 131–140, 1997, doi: 10.1016/0149-1970(96)00007-8.

[16] A. D. Pasternak i D. R. Oander, „Ernest 0. Lawrence Radiation Laboratory".

[17] A. D. Pasternak i D. R. Olander, „LIQUID METAL EXTRACTION OP LANTHANUM AND BARIUM FROM THE URANIUM-CHROMIUM EUTECTIC BY MAGNESIUM, Part I - Solute Distribution", 1966, https://escholarship.org/uc/item/531562zv

[18] A. D. Pasternak, „LIQUID METAL EXTRACTION OF FISSION PRODUCTS FROM URANIUM REACTOR FUELS”, 1966, https://escholarship.org/uc/item/3jg068vz

[19] M. Kieser, H. Muscher, A. Weisenburger, A. Heinzel, i G. Müller, „Liquid metal corrosion/erosion investigations of structure materials in lead cooled systems: Part 1”, *Journal of Nuclear Materials*, 392, nr 3, s. 405–412, 2009, doi: 10.1016/j.jnucmat.2008.12.327.

[20] Y. Katoh *i in.*, „Current status and recent research achievements in SiC/SiC composites”, *Journal of Nuclear Materials*, 455, nr 1–3, s. 387–397, 2014, doi: 10.1016/j.jnucmat.2014.06.003.

[21] M. J. Jackson i J. P. Davim, Red., *Machining with Abrasives*. Boston, MA: Springer US, 2011. doi: 10.1007/978-1-4419-7302-3.

[22] Q. Y. Huang *i in.*, „Corrosion Experiments of the Candidate Materials for Liquid Lithium Lead Blanket of Fusion Reactor”, Materials Challenges for Future Nuclear Fission and Fusion Technologies, 2010, s. 41–50. doi: 10.4028/www.scientific.net/AST.73.41.

[23] M. Caro, K. Woloshun, F. Rubio, S. A. Maloy, i P. Hosemann, „Heavy Liquid Metal Corrosion of Structural Materials in Advanced Nuclear Systems”, *JOM*, t. 65, nr 8, s. 1057–1066, 2013, doi: 10.1007/s11837-013-0663-7.

[24] C. TANG, Y. TANG, J. ZHU, X. QIU, J. LI, i S. XU, „Research and Development of Fuel Element for Chinese 10 MW High Temperature Gas-cooled Reactor”, *Journal of Nuclear Science and Technology*, 37, nr 9, s. 802–806, 2000, doi: 10.1080/18811248.2000.9714959.

[25] E. López-Honorato, J. Tan, P. J. Meadows, G. Marsh, i P. Xiao, „TRISO coated fuel particles with enhanced SiC properties”, *Journal of Nuclear Materials*, 392, nr 2, s. 219–224, 2009, doi: 10.1016/j.jnucmat.2009.03.013.

[26] J. Li *i in.*, „Effect of irradiation damage on corrosion of 4H-SiC in FLiNaK molten salt”, *Corrosion Science*, 125, s. 194–197, 2017, doi: 10.1016/j.corsci.2017.05.028.

[27] H. V. Pham, M. Kurata, i M. Steinbrueck, „Steam Oxidation of Silicon Carbide at High Temperatures for the Application as Accident Tolerant Fuel Cladding, an Overview”, *Thermo*, 1, nr 2, s. 151–167, 2021, doi: 10.3390/thermo1020011.

[28] J. Y. Park, „SiCf/SiC composites as core materials for Generation IV nuclear reactors”, w *Structural Materials for Generation IV Nuclear Reactors*, Elsevier, 2017, s. 441–470. doi: 10.1016/B978-0-08-100906-2.00012-4.

[29] M. E. Levinštejn, S. L. Rumyantsev, i M. Shur, Red., *Properties of advanced semiconductor materials GaN, AlN, InN, BN, SiC, SiGe*. w A Wiley-Interscience publication. New York Weinheim: Wiley, 2001.

[30] J. Lamon, „Properties and Characteristics of SiC and SiC/SiC Composites”, w *Comprehensive Nuclear Materials*, Elsevier, 2012, s. 323–338. doi: 10.1016/B978-0-08-056033-5.00022-7.

[31] L. L. Snead, T. Nozawa, Y. Katoh, T.-S. Byun, S. Kondo, i D. A. Petti, „Handbook of SiC properties for fuel performance modelling”, *Journal of Nuclear Materials*, 371, nr 1–3, s. 329–377, 2007, doi: 10.1016/j.jnucmat.2007.05.016.

[32] T. M. Besmann, D. P. Stinton, R. A. Lowden, i W. Y. Lee, „Chemical Vapor Deposition (CVD) and Infiltration (CVI)”, w *Carbide, Nitride and Boride Materials Synthesis and Processing*, A. W. Weimer, Red., Dordrecht: Springer Netherlands, 1997, s. 547–577. doi: 10.1007/978-94-009-0071-4_22.

[33] J.-J. Huang, C. Militzer, C. Wijayawardhana, U. Forsberg, i H. Pedersen, „Conformal and superconformal chemical vapor deposition of silicon carbide coatings”, *Journal of Vacuum Science & Technology A*, 40, nr 5, s. 053402, 2022, doi: 10.1116/6.0001909.

[34] R. Naslain, F. Langlais, i R. Fedou, „THE CVI-PROCESSING OF CERAMIC MATRIX COMPOSITES”, *J. Phys. Colloques*, 50, nr C5, s. C5-191-C5-207, 1989, doi: 10.1051/jphyscol:1989526.

[35] W.-J. Kim, J. N. Park, M. S. Cho, i J. Y. Park, „Effect of coating temperature on properties of the SiC layer in TRISO-coated particles”, *Journal of Nuclear Materials*, 392, nr 2, s. 213–218, 2009, doi: 10.1016/j.jnucmat.2009.03.012.

[36] A. Lazzeri, „CVI Processing of Ceramic Matrix Composites”, w *Ceramics and Composites Processing Methods*, 1. wyd., N. P. Bansal i A. R. Boccaccini, Red., Wiley, 2012, s. 313–349. doi: 10.1002/9781118176665.ch9.

[37] J. A. DiCarlo i H.-M. Yun, „Non-oxide (Silicon Carbide) Fibers”, w *Handbook of Ceramic Composites*, N. P. Bansal, Red., Springer US, 2005, s. 33–52. doi: 10.1007/0-387-23986-3_2.

[38] Y. Katoh *i in.*, „Continuous SiC fiber, CVI SiC matrix composites for nuclear applications: Properties and irradiation effects”, *Journal of Nuclear Materials*, 448, nr 1–3, s. 448–476, 2014, doi: 10.1016/j.jnucmat.2013.06.040.

[39] C. Sauder, A. Brusson, i J. Lamon, „Influence of Interface Characteristics on the Mechanical Properties of Hi-Nicalon type-S or Tyranno-SA3 Fiber-Reinforced SiC/SiC Minicomposites”, *Int J Applied Ceramic Tech*, 7, nr 3, s. 291–303, 2010, doi: 10.1111/j.1744-7402.2010.02485.x.

[40] H. Tunison, „Compatibility of SiC and SiC Composites with Molten Lead”, UNT Digital Library. https://digital.library.unt.edu/ark:/67531/metadc873616/

[41] I. A. E. Agency, „Challenges for Coolants in Fast Neutron Spectrum Systems”, International Atomic Energy Agency, Text, 2020. https://www.iaea.org/publications/13657/challenges-for-coolants-in-fast-neutron-spectrum-systems

[42] A. Z. Mesquita, *Current Research in Nuclear Reactor Technology in Brazil and Worldwide*. 2013. doi: 10.5772/56032.

[43] G. I. Toshinsky, A. V. Dedul, O. G. Komlev, A. V. Kondaurov, i V. V. Petrochenko, „Lead-Bismuth and Lead as Coolants for Fast Reactors”, *WJNST*, 10, nr 02, s. 65–75, 2020, doi: 10.4236/wjnst.2020.102007.

[44] OECD i Nuclear Energy Agency, *Handbook on Lead-bismuth Eutectic Alloy and Lead Properties, Materials Compatibility, Thermalhydraulics and Technologies*. w Nuclear Science. OECD, 2015. doi: 10.1787/42dcd531-en.

[45] M. Venkatraman, J. P. Neumann, i D. E. Peterson, „The Cr-U (Chromium-Uranium) system”, *Bulletin of Alloy Phase Diagrams*, 6, nr 5, s. 425–429, 1985, doi: 10.1007/BF02869502.

[46] A. Berche, N. Dupin, C. Guéneau, C. Rado, B. Sundman, i J. C. Dumas, „Calphad thermodynamic description of some binary systems involving U”, *Journal of Nuclear Materials*, 411, nr 1–3, s. 131–143, 2011, doi: 10.1016/j.jnucmat.2011.01.043.

[47] H. A. Saller i F. A. Rough, „Alloys of Uranium with Zirconium, Chromium, Columbium, Vanadium, and Molybdenum”, UNT Digital Library. https://digital.library.unt.edu/ark:/67531/metadc502544/

[48] J. S. Finucane, „THE VISCOSITY OF URANIUM METAL AND SOME URAWIUM-CHROVIIUM ALLOYS”, 1969, https://escholarship.org/uc/item/96j3r0n0

[49] J. M. McKee, Jr., „Thermal conductivity of uranium-chromiu and uranium-iron eutectic alloys”. https://www.osti.gov/servlets/purl/4360137

[50] R. A. (Rutgers USA) McCauley, *Corrosion of Ceramic Materials*. Boca Raton, FL, 2013.

[51] E. Heitz, „Mechanistically based prevention strategies of flow-induced corrosion”, *Electrochimica Acta*, 41, nr 4, s. 503–509, 1996, doi: 10.1016/0013-4686(95)00336-3.

[52] C. Fazio i F. Balbaud, „Corrosion phenomena induced by liquid metals in Generation IV reactors”, w *Structural Materials for Generation IV Nuclear Reactors*, Elsevier, 2017, s. 23–74. doi: 10.1016/B978-0-08-100906-2.00002-1.

[53] O. Ruff i B. Bergdahl, „Arbeiten im Gebiet hoher Temperaturen. XII. Die Messung von Dampfspannungen bei sehr hohen Temperaturen nebst einigen Beobachtungen über die Löslichkeit von Kohlenstoff in Metallen”, *Z. Anorg. Allg. Chem.*, 106, nr 1, s. 76–94, 1919, doi: 10.1002/zaac.19191060107.

[54] D. H. Kirkwood i J. Chipman, „THE FREE ENERGY OF SILICON CARBIDE FROM ITS SOLUBILITY IN MOLTEN LEAD”, 65:1082 http://lib3.dss.go.th/fulltext/scan_ebook/j.of_physical_1961_v65_n6.pdf

[55] C. D. Thurmond i M. Kowalchik, „Germanium and Silicon Liquidus Curves”, *Bell System Technical Journal*, 39, nr 1, s. 169–204, 1960, doi: 10.1002/j.1538-7305.1960.tb03927.x.

[56] M. Sauzay, „Mechanical behavior of structural materials for Generation IV reactors”, w *Structural Materials for Generation IV Nuclear Reactors*, Elsevier, 2017, s. 191–252. doi: 10.1016/B978-0-08-100906-2.00006-9.

[57] J. B. Malherbe, „Diffusion of fission products and radiation damage in SiC”, *J. Phys. D: Appl. Phys.*, 46, nr 47, s. 473001, 2013, doi: 10.1088/0022-3727/46/47/473001.

[58] E. Kucal, K. Czerski, i Z. Kozioł, „Molecular Dynamics Simulations of Primary Radiation Damage in Silicon Carbide”, *Acta Phys. Pol. A*, 142, nr 6, s. 747–752, 2022, doi: 10.12693/APhysPolA.142.747.

[59] Y. Katoh *i in.*, „Current status and critical issues for development of SiC composites for fusion applications”, *Journal of Nuclear Materials*, 367–370, s. 659–671, 2007, doi: 10.1016/j.jnucmat.2007.03.032.

[60] A. Aitkaliyeva, L. He, H. Wen, B. Miller, X. M. Bai, i T. Allen, „Irradiation effects in Generation IV nuclear reactor materials”, w *Structural Materials for Generation IV Nuclear Reactors*, Elsevier, 2017, s. 253–283. doi: 10.1016/B978-0-08-100906-2.00007-0.

[61] C. H. Henager, „Swelling and time-dependent crack growth in SiC/SiC composites”, *Journal of Nuclear Materials*, 367–370, s. 742–747, 2007, doi: 10.1016/j.jnucmat.2007.03.088.

[62] C. Henager, „Subcritical crack growth in CVI SiCf/SiC composites at elevated temperatures: effect of fiber creep rate”, *Acta Materialia*, 49, nr 18, s. 3727–3738, 2001, doi: 10.1016/S1359-6454(01)00276-2.

[63] P. Chakraborty, A. Ghosh, i G. Dey, „Compatibility of Lead-Bismuth Eutectic with SiC-Coated Graphite at Elevated Temperature”, *Metallurgical and Materials Transactions B*, 48, 2016, doi: 10.1007/s11663-016-0763-1.

[64] K. Nogi i K. Ogino, „Wettability of Sic by Liquid Pure Metals”, *Trans. JIM*, 29, nr 9, s. 742–747, 1988, doi: 10.2320/matertrans1960.29.742.

[65] J. C. Clifford, „A loop for circulating liquid lead-bismuth mixtures: corrosion studies and operation”.

[66] W. H. Cook, „CORROSION RESISTANCE OF VARIOUS CERAMICS AND CERMETS TO LIQUID METALS”, ORNL-2391, 4142090, 1960. doi: 10.2172/4142090.

[67] C. Park, K. Noborio, R. Kasada, Y. Yamamoto, i S. Konishi, „Compatibility of SiCf/SiC composite exposed to liquid Pb–Li flow", *Journal of Nuclear Materials*, 417, nr 1–3, s. 1218–1220, 2011, doi: 10.1016/j.jnucmat.2011.06.016.

[68] J. Stromsoe, „High Temperature Liquid Metal Loop".

[69] B. Li *i in.*, „Dissolution corrosion of 4H-SiC in lead-bismuth eutectic at 550°C", *Materials and Corrosion*, 70, nr 10, s. 1878–1883, 2019, doi: 10.1002/maco.201910777.

[70] F. Barbier, Ph. Deloffre, i A. Terlain, „Compatibility of materials for fusion reactors with Pb–17Li", *Journal of Nuclear Materials*, 307–311, s. 1351–1354, 2002, doi: 10.1016/S0022-3115(02)00987-X.

[71] J. Hui, B.-L. Zhang, T. Liu, M. Liu, i W.-G. Liu, „Effects of impurity elements on SiC grain boundary stability and corrosion", *NUCL SCI TECH*, 32, nr 11, s. 125, 2021, doi: 10.1007/s41365-021-00963-2.

[72] C. Park, „Study on Compatibility of Advanced Materials Exposed to Liquid Pb-Li for High Temperature Blanket System". Kyoto University, 2013. doi: 10.14989/doctor.k17916.

[73] B. A. Pint, J. L. Moser, i P. F. Tortorelli, „Investigation of Pb–Li compatibility issues for the dual coolant blanket concept", *Journal of Nuclear Materials*, 367–370, s. 1150–1154, 2007, doi: 10.1016/j.jnucmat.2007.03.206.

[74] C. Si *i in.*, „Review on The Compatibility of Fusion Reactor Structural Materials with High-temperature Liquid Metals", *J. Phys.: Conf. Ser.*, 1637, s. 012037, 2020, doi: 10.1088/1742-6596/1637/1/012037.

[75] S. Y. Chen i I. D. Boyd, „Chemical equilibrium analysis of silicon carbide oxidation in oxygen and air", *J Am Ceram Soc*, 102, nr 7, s. 4272–4284, 2019, doi: 10.1111/jace.16272.

[76] J. Roy, S. Chandra, S. Das, i S. Maitra, „OXIDATION BEHAVIOUR OF SILICON CARBIDE - A REVIEW".

[77] J. Wang, L. Zhang, Q. Zeng, G. L. Vignoles, i A. Guette, „Theoretical Investigation for the Active-to-Passive Transition in the Oxidation of Silicon Carbide", *J American Ceramic Society*, 91, nr 5, s. 1665–1673, 2008, doi: 10.1111/j.1551-2916.2008.02353.x.

[78] S. B. Lyon, „Corrosion of Molybdenum and its Alloys", w *Shreir's Corrosion*, Elsevier, 2010, s. 2157–2167. doi: 10.1016/B978-044452787-5.00106-2.

[79] Z. Zheng, R. E. Tressler, i K. E. Spear, „Oxidation of Single-Crystal Silicon Carbide: Part I . Experimental Studies", *J. Electrochem. Soc.*, 137, nr 3, s. 854–858, 1990, doi: 10.1149/1.2086568.

[80] Z. Zheng, R. E. Tressler, i K. E. Spear, „Oxidation of Single-Crystal Silicon Carbide: Part II . Kinetic Model", *J. Electrochem. Soc.*, 137, nr 9, s. 2812–2816, 1990, doi: 10.1149/1.2087080.

[81] I. Vickridge, J. Ganem, Y. Hoshino, i I. Trimaille, „Growth of SiO_2 on SiC by dry thermal oxidation: mechanisms", *J. Phys. D: Appl. Phys.*, 40, nr 20, s. 6254–6263, 2007, doi: 10.1088/0022-3727/40/20/S10.

[82] J. R. Blachere, F. S. Pettit, i B. S. Terry, „High Temperature Corrosion of Ceramics", *High Temperature Technology*, 8, nr 2, s. 175–175, 1990, doi: 10.1080/02619180.1990.11753475.

[83] A. Heinzel, A. Weisenburger, i G. Müller, „Long-term corrosion tests of Ti 3 SiC 2 and Ti 2 AlC in oxygen containing LBE at temperatures up to 700 °C", *Journal of Nuclear Materials*, 482, s. 114–123, 2016, doi: 10.1016/j.jnucmat.2016.10.007.

[84] C. A. Colmenares, „The oxidation of thorium, uranium, and plutonium", *Progress in Solid State Chemistry*, 9, s. 139–239, 1975, doi: 10.1016/0079-6786(75)90016-3.

[85] B. P. Burylev, V. E. Kritskii, S. N. Gavrilov, i E. B. Kritskaya, „Solubility of oxygen in chromium–nickel steels", *Welding International*, 20, nr 11, s. 910–912, 2006, doi: 10.1533/wint.2006.3712.

[86] R. Ganesan, T. Gnanasekaran, i R. S. Srinivasa, „Diffusivity, activity and solubility of oxygen in liquid lead and lead–bismuth eutectic alloy by electrochemical methods”, *Journal of Nuclear Materials*, 349, nr 1–2, s. 133–149, 2006, doi: 10.1016/j.jnucmat.2005.10.006.

[87] E. J. Opila i N. S. Jacobson, „Corrosion of Ceramic Materials”, w *Materials Science and Technology: A Comprehensive Treatment*, 1. wyd., R. W. Cahn, P. Haasen, i E. J. Kramer, Red., Wiley, 2000, s. 327–388. doi: 10.1002/9783527619306.ch16.

[88] H. Xue *i in.*, „Ag out-surface diffusion in crystalline SiC with an effective SiO2 diffusion barrier”, *Journal of Nuclear Materials*, 464, s. 294–298, 2015, doi: 10.1016/j.jnucmat.2015.05.001.

[89] P. J. Jorgensen, M. E. Wadsworth, i I. B. Cutler, „Oxidation of Silicon Carbide”, *J American Ceramic Society*, 42, nr 12, s. 613–616, 1959, doi: 10.1111/j.1151-2916.1959.tb13582.x.

[90] Y. K. Sharma, „Advanced SiC/Oxide Interface Passivation”, w *New Research on Silicon - Structure, Properties, Technology*, V. I. Talanin, Red., InTech, 2017. doi: 10.5772/67867.

[91] R. G. Munro i S. J. Dapkunas, „Corrosion characteristics of silicon carbide and silicon nitride”, *J. RES. NATL. INST. STAN.*, 98, nr 5, s. 607, 1993, doi: 10.6028/jres.098.040.

[92] G. L. Hofman i L. C. Walters, „1 Metallic Fast Reactor Fuels”.

[93] Thomas C. Allison, „NIST-JANAF Thermochemical Tables - SRD 13”. National Institute of Standards and Technology, 2013. doi: 10.18434/T42S31.

[94] C. Varadachari, R. Bhowmick, i K. Ghosh, „Thermodynamics and Oxidation Behaviour of Crystalline Silicon Carbide (3C) with Atomic Oxygen and Ozone”, *ISRN Thermodynamics*, 2012, s. 1–8, 2012, doi: 10.5402/2012/108781.

[95] N. Baghdasaryan i T. Kozlowski, „Review of Progress in Coated Fuel Particle Performance Analysis”, *Nuclear Science and Engineering*, 194, nr 3, s. 169–180, 2020, doi: 10.1080/00295639.2019.1686882.

[96] J. S. Morrell i M. J. Jackson, *Uranium Processing and Properties*. Springer Science & Business Media, 2013.

[97] N. R. Gubel, „Investigation of liquid uranium-ceramic corrosion kinetics for metal fuel processing”, 2012, https://repository.mines.edu/handle/11124/16661

[98] E. B. Ripley, „Melting and Casting of Uranium”, w *Uranium Processing and Properties*, J. S. Morrell i M. J. Jackson, Red., New York, NY: Springer New York, 2013, s. 35–69. doi: 10.1007/978-1-4614-7591-0_2.

[99] T. Ulrich, „Modeling the Uranium-Silicon Phase Equilibria Based on Computational and Experimental Analysis”, *Theses and Dissertations*, 2019, https://scholarcommons.sc.edu/etd/5515

[100] M. Hansen, K. Anderko, i H. W. Salzberg, „Constitution of Binary Alloys”, *J. Electrochem. Soc.*, 105, nr 12, s. 260C, 1958, doi: 10.1149/1.2428700.

[101] K. Bhanumurthy i R. Schmid-Fetzer, „Interface reactions between silicon carbide and metals (Ni, Cr, Pd, Zr)”, *Composites Part A: Applied Science and Manufacturing*, 32, nr 3–4, s. 569–574, 2001, doi: 10.1016/S1359-835X(00)00049-X.

[102] M. Vlasova *i in.*, „Mechanoactivation of chromium silicide formation in the SiC-Cr-Si system”, *Sci Sintering*, 34, nr 3, s. 231–240, 2002, doi: 10.2298/SOS0203231V.

[103] J. R. Ch, E. Vetrivendan, B. Madhura, i S. Ningshen, „A review of ceramic coatings for high temperature uranium melting applications”, *Journal of Nuclear Materials*, 540, s. 152354, 2020, doi: 10.1016/j.jnucmat.2020.152354.

[104] S. K. Sharma, M. T. Saify, S. Majumdar, i P. K. Mollick, „Interaction study of molten uranium with multilayer SiC/Y2O3 and Mo/Y2O3 coated graphite", *Nuclear Engineering and Technology*, 55, nr 5, s. 1855–1862, 2023, doi: 10.1016/j.net.2022.12.025.

[105] G.-M. Song, Y. Zhou, S.-J. L. Kang, i D.-Y. Yoon, „Effect of carbon fibers on the thermophysical properties of TiC composites", *Journal of Materials Science Letters*, 21, nr 22, s. 1733–1736, 2002, doi: 10.1023/A:1020948132154.

[106] Y. Katoh, G. Vasudevamurthy, T. Nozawa, i L. L. Snead, „Properties of zirconium carbide for nuclear fuel applications", *Journal of Nuclear Materials*, 441, nr 1–3, s. 718–742, 2013, doi: 10.1016/j.jnucmat.2013.05.037.

[107] K. Minato *i in.*, „Fission product release from ZrC-coated fuel particles during postirradiation heating at 1600°C", *Journal of Nuclear Materials*, 224, nr 1, s. 85–92, 1995, doi: 10.1016/0022-3115(95)00032-1.

[108] B. A. Pint, J. Jun, i M. Romedenne, „Compatibility of SiC with ODS FeCrAl in flowing Pb-Li at 600°–700 °C", *Fusion Engineering and Design*, 166, s. 112389, 2021, doi: 10.1016/j.fusengdes.2021.112389.

[109] L.-X. Wu *i in.*, „Nano-infiltration and transient eutectic (NITE) phase joining SiC ceramics at 1500oC", *Ceramics International*, 45, nr 18, Part A, s. 24927–24931, 2019, doi: 10.1016/j.ceramint.2019.08.193.

[110] Y. Taki, M. Kitiwan, H. Katsui, i T. Goto, „Electrical and thermal properties of off-stoichiometric SiC prepared by spark plasma sintering", *Journal of Asian Ceramic Societies*, 6, nr 1, s. 95–101, 2018, doi: 10.1080/21870764.2018.1446490.

[111] Y. Lei *i in.*, „Simulation and experimental studies of the dissolution corrosion of 4H-SiC in liquid Pb/Bi", *Applied Surface Science*, 585, s. 152686, 2022, doi: 10.1016/j.apsusc.2022.152686.

[112] P. Hohenberg i W. Kohn, „Inhomogeneous Electron Gas", *Phys. Rev.*, 136, nr 3B, s. B864–B871, 1964, doi: 10.1103/PhysRev.136.B864.

[113] W. Kohn i L. J. Sham, „Self-Consistent Equations Including Exchange and Correlation Effects", *Phys. Rev.*, 140, nr 4A, s. A1133–A1138, 1965, doi: 10.1103/PhysRev.140.A1133.

[114] D. S. Sholl i J. A. Steckel, *Density Functional Theory: A Practical Introduction*, 1. wyd. Wiley, 2009. doi: 10.1002/9780470447710.

[115] A. Hamed Mashhadzadeh, M. Ghorbanzadeh Ahangari, A. Salmankhani, i M. Fataliyan, „Density functional theory study of adsorption properties of non-carbon, carbon and functionalized graphene surfaces towards the zinc and lead atoms", *Physica E: Low-dimensional Systems and Nanostructures*, 104, s. 275–285, 2018, doi: 10.1016/j.physe.2018.08.010.

[116] A. Visikovskiy, S. Hayashi, T. Kajiwara, F. Komori, K. Yaji, i S. Tanaka, „Computational study of heavy group IV elements (Ge, Sn, Pb) triangular lattice atomic layers on SiC(0001) surface". arXiv, 4 wrzesień 2018. http://arxiv.org/abs/1809.00829

[117] W. H. Lee i X. H. Yao, „First principle investigation of phase transition and thermodynamic properties of SiC", *Computational Materials Science*, 106, s. 76–82, 2015, doi: 10.1016/j.commatsci.2015.04.044.

[118] H. Braekken, „Zur Kristallstruktur des kubischen Karborunds". https://www.crystallography.net/cod/1010995.html

[119] K. Momma i F. Izumi, „VESTA 3 for three-dimensional visualization of crystal, volumetric and morphology data", *J Appl Cryst*, 44, nr 6, Art. nr 6, 2011, doi: 10.1107/S0021889811038970.

[120] L. Pizzagalli, „Accurate values of 3C, 2H, 4H, and 6H SiC elastic constants using DFT calculations and heuristic errors corrections”, *Philosophical Magazine Letters*, 101, nr 6, s. 242–252, 2021, doi: 10.1080/09500839.2021.1909167.

[121] J. Pollmann i P. Krüger, „Reconstruction models of cubic SiC surfaces”, *J. Phys.: Condens. Matter*, 16, nr 17, s. S1659–S1703, 2004, doi: 10.1088/0953-8984/16/17/012.

[122] V. Y. Aristov, „β-SiC(100) surface: atomic structures and electronic properties”, *Phys.-Usp.*, 44, nr 8, s. 761, 2001, doi: 10.1070/PU2001v044n08ABEH000979.

[123] A. Catellani, G. Galli, i F. Gygi, „Reconstruction and Thermal Stability of the Cubic SiC (001) Surfaces”, *Phys. Rev. Lett.*, 77, nr 25, s. 5090–5093, 1996, doi: 10.1103/PhysRevLett.77.5090.

[124] A. Catellani i G. Cicero, „Modifications of cubic SiC surfaces studied by *ab initio* simulations: from gas adsorption to organic functionalization”, *J. Phys. D: Appl. Phys.*, 40, nr 20, s. 6215–6224, 2007, doi: 10.1088/0022-3727/40/20/S07.

[125] A. Konopka *i in.*, „Paramagnetic signature of microcrystalline silicon carbide”, *IOP Conf. Ser.: Mater. Sci. Eng.*, 15, nr 1, s. 012013, 2010, doi: 10.1088/1757-899X/15/1/012013.

[126] W. Gordy i W. J. O. Thomas, „Electronegativities of the Elements”, *The Journal of Chemical Physics*, 24, nr 2, s. 439–444, 1956, doi: 10.1063/1.1742493.

[127] J. P. Cottom, „The Characterisation of Performance Limiting Defects in 4H-SiC Devices using Density Functional Theory”.

[128] D. Frenkel i B. Smit, *Understanding Molecular Simulation*. Elsevier, 2002. doi: 10.1016/B978-0-12-267351-1.X5000-7.

[129] A. P. Thompson *i in.*, „LAMMPS - a flexible simulation tool for particle-based materials modeling at the atomic, meso, and continuum scales”, *Computer Physics Communications*, 271, s. 108171, 2022, doi: 10.1016/j.cpc.2021.108171.

[130] J. Tersoff, „Modeling solid-state chemistry: Interatomic potentials for multicomponent systems”, *Phys. Rev. B*, 39, nr 8, s. 5566–5568, 1989, doi: 10.1103/PhysRevB.39.5566.

[131] S. Munetoh, T. Motooka, K. Moriguchi, i A. Shintani, „Interatomic potential for Si-O systems using Tersoff parameterization”, *Computational Materials Science*, 39, nr 2, s. 334–339, 2007, doi: 10.1016/j.commatsci.2006.06.010.

[132] J. Lennard-Jones, „Efficient «universal» shifted Lennard-Jones model for all KIM API supported species developed by Elliott and Akerson (2015) v003”. OpenKIM, 2018. doi: 10.25950/962B4967.

[133] J. E. Lennard-Jones i S. Chapman, „On the forces between atoms and ions”, *Proceedings of the Royal Society of London. Series A, Containing Papers of a Mathematical and Physical Character*, 109, nr 752, s. 584–597, 1997, doi: 10.1098/rspa.1925.0147.

[134] „Ueber die Anwendung des Satzes vom Virial in der kinetischen Theorie der Gase”, s. 127–136, 1881, doi: 10.1002/andp.18812480110.

[135] Q. Wang, N. Gui, X. Zhang, X. Yang, J. Tu, i S. Jiang, „Diffusion and thermo-driven migration of silver, palladium, and ruthenium nanoparticles in cubic SiC matrix using molecular dynamics”, *International Journal of Heat and Mass Transfer*, 197, s. 123359, 2022, doi: 10.1016/j.ijheatmasstransfer.2022.123359.

[136] A. P. Bartók, J. Kermode, N. Bernstein, i G. Csányi, „Machine Learning a General-Purpose Interatomic Potential for Silicon”, *Phys. Rev. X*, 8, nr 4, s. 041048, 2018, doi: 10.1103/PhysRevX.8.041048.

[137] A. P. Bartók *i in.*, „Machine learning unifies the modeling of materials and molecules”, *Sci. Adv.*, 3, nr 12, s. e1701816, 2017, doi: 10.1126/sciadv.1701816.

[138] J. A. Keith *i in.*, „Combining Machine Learning and Computational Chemistry for Predictive Insights Into Chemical Systems”, *Chem. Rev.*, 121, nr 16, s. 9816–9872, 2021, doi: 10.1021/acs.chemrev.1c00107.

[139] Y. Miao, K. Mo, T. Fei, i Y. Cao, „Multiphysics simulations of Self-Regulating performance of an optimized molten metal fuel microreactor design”, *Nuclear Engineering and Design*, 406, s. 112244, 2023, doi: 10.1016/j.nucengdes.2023.112244.

[140] Q. Wu i J. J. Sienicki, „Stability analysis on single-phase natural circulation in Argonne lead loop facility”, *Nuclear Engineering and Design*, 224, nr 1, s. 23–32, 2003, doi: 10.1016/S0029-5493(03)00099-2.

[141] A. V. Zhukov, J. A. Kuzina, V. A. Uhov, i G. A. Sorokin, „NATURAL CONVECTION AS THE WAY OF HEAT REMOVAL FROM FAST REACTOR CORE AT COOLDOWN REGIMES”.

[142] D. Grishchenko, M. Jeltsov, K. Kööp, A. Karbojian, W. Villanueva, i P. Kudinov, „The TALL-3D facility design and commissioning tests for validation of coupled STH and CFD codes”, *Nuclear Engineering and Design*, 290, s. 144–153, 2015, doi: 10.1016/j.nucengdes.2014.11.045.

[143] W. Ma, A. Karbojian, i B. R. Sehgal, „Experimental study on natural circulation and its stability in a heavy liquid metal loop”, *Nuclear Engineering and Design*, 237, nr 15–17, s. 1838–1847, 2007, doi: 10.1016/j.nucengdes.2007.02.023.

[144] B. R. Sehgal, W. M. Ma, i A. Karbojian, „Lead-Bismuth Flow and Heat Transfer Performance in Heat Exchangers”.

[145] G. Chen, J. Wang, H. Zhang, L. Li, i H. Fan, „Low-temperature oxy-nitriding of 316 L austenitic stainless steel for improved corrosion resistance in liquid lead-bismuth eutectic”, *Scripta Materialia*, 202, s. 114014, 2021, doi: 10.1016/j.scriptamat.2021.114014.

[146] X. Li, „Heat Exchangers for the Next Generation of Nuclear Reactors”, 2006.

[147] S.-J. Yoon, P. Sabharwall, i E.-S. Kim, „Analytical Study on Thermal and Mechanical Design of Printed Circuit Heat Exchanger”, INL/EXT--13-30047, 1116746, 2013. doi: 10.2172/1116746.

[148] T. Dixit, E. Al-Hajri, M. C. Paul, P. Nithiarasu, i S. Kumar, „High performance, microarchitected, compact heat exchanger enabled by 3D printing”, *Applied Thermal Engineering*, 210, s. 118339, 2022, doi: 10.1016/j.applthermaleng.2022.118339.

[149] L. Melchiorri, V. Narcisi, F. Giannetti, G. Caruso, i A. Tassone, „Development of a RELAP5/MOD3.3 Module for MHD Pressure Drop Analysis in Liquid Metals Loops: Verification and Validation”, *Energies*, 14, nr 17, Art. nr 17, 2021, doi: 10.3390/en14175538.

[150] S. Eckert, A. Cramer, i G. Gerbeth, „Velocity Measurement Techniques for Liquid Metal Flows”, w *Magnetohydrodynamics*, 80, w Fluid Mechanics And Its Applications, vol. 80. , Dordrecht: Springer Netherlands, 2007, s. 275–294. doi: 10.1007/978-1-4020-4833-3_17.

[151] M. Ratajczak *i in.*, „Measurement techniques for liquid metals”, *IOP Conf. Ser.: Mater. Sci. Eng.*, 228, s. 012023, 2017, doi: 10.1088/1757-899X/228/1/012023.

[152] A. Thess, E. Votyakov, B. Knaepen, i O. Zikanov, „Theory of the Lorentz force flowmeter”, *New Journal of Physics*, 9, s. 299, 2007, doi: 10.1088/1367-2630/9/8/299.

[153] A. Thess, Y. Kolesnikov, C. Karcher, i E. Votyakov, „Lorentz Force Velocimetry – A Contactless Technique for Flow Measurement in High-Temperature Melts”.

[154] S. Eckert, G. Gerbeth, i V. I. Melnikov, „ULTRASONIC VELOCITY MEASUREMENTS IN LIQUID METALS USING ACOUSTIC WAVE GUIDES”.

[155] S. Eckert i G. Gerbeth, „Velocity measurements in liquid metal flows using the Ultrasonic Doppler Method: examples and perspectives”.

[156] J. Lim, G. Manfredi, K. Rosseel, i A. Aerts, „Performance of Electrochemical Oxygen Pump in a Liquid Lead-Bismuth Eutectic Loop”, *J. Electrochem. Soc.*, 166, nr 6, s. E153–E158, 2019, doi: 10.1149/2.0711906jes.

[157] J. Lim, G. Manfredi, S. Gavrilov, K. Rosseel, A. Aerts, i J. Van den Bosch, „Control of dissolved oxygen in liquid LBE by electrochemical oxygen pumping”, *Sensors and Actuators B: Chemical*, 204, s. 388–392, 2014, doi: 10.1016/j.snb.2014.07.117.

[158] J.-L. Courouau, „Electrochemical oxygen sensors for on-line monitoring in lead–bismuth alloys: status of development”, *Journal of Nuclear Materials*, 335, nr 2, s. 254–259, 2004, doi: 10.1016/j.jnucmat.2004.07.020.

[159] J.-L. Courouau *i in.*, „Impurities and oxygen control in lead alloys”, *Journal of Nuclear Materials*, 301, nr 1, s. 53–59, 2002, doi: 10.1016/S0022-3115(01)00726-7.

[160] G. Müller, G. Schumacher, i F. Zimmermann, „Investigation on oxygen controlled liquid lead corrosion of surface treated steels”, *Journal of Nuclear Materials*, 278, nr 1, s. 85–95, 2000, doi: 10.1016/S0022-3115(99)00211-1.

[161] H. Shi *i in.*, „Corrosion resistance and microstructural stability of austenitic Fe–Cr–Al–Ni model alloys exposed to oxygen-containing molten lead”, *Journal of Nuclear Materials*, 524, s. 177–190, 2019, doi: 10.1016/j.jnucmat.2019.06.043.

[162] J. Zhang i N. Li, „Analysis on liquid metal corrosion–oxidation interactions”, *Corrosion Science*, 49, nr 11, s. 4154–4184, 2007, doi: 10.1016/j.corsci.2007.05.012.

[163] H. Glasbrenner, J. Konys, G. Mueller, i A. Rusanov, „Corrosion investigations of steels in ¯owing lead at 400°C and 550°C”, *Journal of Nuclear Materials*, 2001.

[164] C. Li *i in.*, „A synergy of different corrosion failure modes pertaining to T91 steel impacted by extreme lead–bismuth eutectic flow pattern”, *Corrosion Science*, 180, s. 109214, 2021, doi: 10.1016/j.corsci.2020.109214.

[165] G. Müller *i in.*, „Results of steel corrosion tests in flowing liquid Pb/Bi at 420–600 °C after 2000 h”, *Journal of Nuclear Materials*, 301, nr 1, s. 40–46, 2002, doi: 10.1016/S0022-3115(01)00725-5.

[166] E. Yamaki, K. Ginestar, i L. Martinelli, „Dissolution mechanism of 316L in lead–bismuth eutectic at 500 °C”, *Corrosion Science*, 53, nr 10, s. 3075–3085, 2011, doi: 10.1016/j.corsci.2011.05.031.